

## SKYNET'S SUITE OF PROCESSING ALGORITHMS FOR SINGLE-DISH RADIO TELESCOPES

JOHN MARTIN<sup>\*</sup>

Physics and Astronomy Department, UNC-Chapel Hill.

27 April 2018

### ABSTRACT

Skynet is an international network of over two dozen optical robotic telescopes operated out of the University of North Carolina at Chapel Hill. In response to recently acquired privileges of the 20-meter diameter radio telescope located at Green Bank Observatory, Skynet has developed a new radio image processing software which hosts a number of advantages over traditional radio image processing techniques. The most noteworthy of these advantages include the use of weighted modeling over weighted averaging—the former being a procedure that blurs astrophysical structure as high as 40%—and the use of local, rather than global, modeling to differentiate astrophysical signal from various forms of radio contaminants. Our algorithm also makes frequent use of robust Chauvenet rejection (RCR), a new outlier rejection algorithm. RCR is capable of resolving both accurate and precise mu and sigma values for distributions containing as high as 85% contaminated data, making it particularly advantageous for removing radio contamination. Together, these techniques produce allow our image processing software to produce contaminant-cleaned and photometrically viable images for professional and amateur use.



FIG. 1.— Green Bank Observatory 20-meter diameter radio telescope. (Photo credit: GBO)

### 1. INTRODUCTION

Skynet is a network of 24 robotic and optical telescopes scattered across four continents that brings students, educators, and professionals access to high-fidelity astronomy equipment through a common web-based interface. Since conceived in 2005, the network has collected over 50,000 users and taken over 15-million images. Consequently, Skynet contributes to diverse research projects, spanning between work on gamma-ray bursts (Reichart et al. 2005, Haislip et al. 2006, Dai et al. 2007, Updike et al. 2008, Nysewander et al. 2009, Cenko et al. 2011, Cano et al. 2011, Bufano et al. 2012, Jin et al. 2013, Morgan et al. 2014, Martin-Carrillo et al. 2014, Friis et al. 2015, De Pasquale et al. 2016, Bardho et al. 2016,

Melandri et al. 2017), variable stars (Layden et al. 2010, Gvaramadze et al. 2012, Wehrung et al. 2013, Miroshnichenko et al. 2014, Abbas et al. 2015, Khokhlov et al. 2017, 2018), pulsating white dwarfs (Thompson et al. 2010, Barlow et al. 2010, 2011, 2013, 2017, Reed et al. 2012, Bourdreaux et al. 2017, Hutchens et al. 2017), supernovae (Foley et al. 2010, 2012, 2013, Pignata et al. 2011, Valenti et al. 2011, 2014, Pastorello et al. 2013, Milisavljevic et al. 2013, Maund et al. 2013, Fraser et al. 2013, Stritzinger et al. 2014, Inserra et al. 2014, Takats et al. 2014, 2015, 2016, Dall’Ora et al. 2014, Folatelli et al. 2014, Barbarino et al. 2015, de Jaeger et al. 2016, Gutierrez et al. 2016, Tartaglia et al. 2017, 2018, Prentice et al. 2017), near-earth objects (Brozovic et al. 2011, Pravec et al. 2014), and even recently the detection of gravitational wave sources (Abbott et al. 2017a, 2017b, Valenti et al. 2017, Yang et al. 2017).

As part of the American Recovery and Reinvestment Act of 2009 and in collaboration with Green Bank Observatory (GBO), Skynet acquired its first radio telescope from GBO: the 20-meter diameter single-dish radio telescope (Figure 1). After updating of the telescope’s hardware in 2010 and integrating the data acquisition software into Skynet, the telescope is now operable by educators, students, and professionals through the Skynet web-interface<sup>2</sup>.

In addition to data acquisition, Skynet also offers in-house processing for images. While professional image processing procedures are well-established for optical telescopes, the same is not true for radio telescopes. As such, Skynet sought to develop equally reliable and powerful processing capabilities for data collected by the new radio telescope. The two primary challenges to building such a processing pipeline for radio images are (1) developing the ability to extract radio contaminants in a user-defined, yet statistically meaningful way, and (2) providing a means to map radio data to a pixel based im-

<sup>\*</sup> The author would like to acknowledge the significant collaboration with his adviser Dr. Daniel Reichart, along with the current and former students and software engineers in the Skynet group, specifically Dylan Dutton, Michael Maples, and Travis Berger.

<sup>2</sup> <http://skynet.unc.edu>

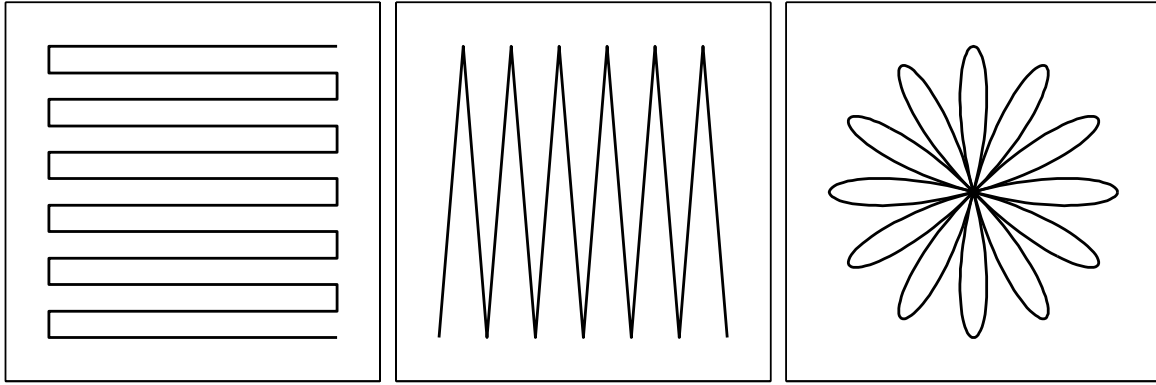


FIG. 2.— Mapping patterns. **Left:** Raster. **Middle:** Nodding. **Right:** Daisy.

age without loosing the resolution capabilities of the telescope. This paper aims to update and validate Skynet’s preliminary solutions to addressing these two challenges (Berger 2015) as well as to introduce additional functionality and robustness to the processing suite for further contaminant reduction and scientific use.

### 1.1. Radio Data Acquisition and Analysis Techniques

Radio telescopes differ from optical telescopes in two primary ways: (1) given the low energy of the photons, the receiver has extremely low resolution and effectively acts as a single pixel would for a optical CCD. (2) As a consequence of the low-resolution receiver, it becomes extremely inefficient and financially nonviable to map an image pixel by pixel. Instead, radio observations are collected as a sparse grid of single pixel measurements which later are interpolated to form a final image. The methods through which these grids are collected are described below.

#### 1.1.1. Mapping Patterns

Because radio telescopes operate using a single-pixel camera receiver, there are two common procedures used to collect the radio data. First is the point-and-shoot method, where the telescope slews point-to-point on a predetermined mapping grid, stopping to integrate at each predetermined location to produce a flux value. The point-and-shoot procedure requires frequent acceleration and deceleration of the telescope—known to cause substantial wear on the telescope mount. The alternative method that Skynet has chosen to employ is an on-the-fly mapping technique where the telescope receiver continues to integrate as the telescope moves. This minimizes the amount of strain experienced by the telescope to start and stop its motion, while also providing greater flexibility for different mapping patterns and a user defined sampling rate (our default is 0.2 beamwidths). Specifically, through on-the-fly mapping, the 20-meter telescope is capable of collecting data in three standard patterns (Figure 2).

- Rasters mapping patterns most closely resemble the rectangular grid utilized by the point-and-shoot method. Here the telescope maintains either a constant right ascension or declination while sampling at a constant interval in the alternative coordinate to produce a single scan. These scans are produced at predetermined intervals across the field of view

to build a survey of individual scans which together form the raster mapping pattern.

- Noddings are mapping patterns that utilize the rotation of the earth to minimize the amount of impulse experienced by the telescope. Popular for meridian-transit telescopes, the pattern slews the telescope parallel to the elevation coordinate thereby utilizing the rotating of the earth to cover the field of view.
- Daisy mapping patterns are the most complex pattern, but also the pattern that puts the least amount of strain on the telescope. By slowly accelerating and decelerating the telescope around the source of interest, the telescope never has an abrupt halt to transition its orientation and collect a new scan. Instead the telescope smoothly transitions from one scan into the next. Another advantage of the daisy pattern is that it can be configured to collect an arbitrarily large number of scans or ‘pedals’ to cross over the source.

Given the variety of mapping patterns, we made it a requirement of our algorithm to be independent of the mapping structure of the observation. So long as gaps between scans do not exceed the Nyquist sampling rate ( $\approx 0.4$  beamwidths), all information can theoretically be recovered.

### 1.2. Signal Averaging vs. Signal Modeling

Some processing algorithms avoid the requirement of point-and-shoot data acquisition by imposing their data onto a rectangular grid through a process called regridding (Winkel, Floer & Kraus 2012). The process involves collecting all local data near the desired grid point and using a weighted average of that local data to interpolate a value onto a location in the sky that may or may not have been sampled. The harm in this approach is the immediate convolution of the original and likely-biased data. This imposed convolution kernel not only propagates uncertainty in ways that are difficult to understand but in ways that are difficult to properly account for. Furthermore, the method blurs the data as high as 40%.

Our solution to this problem is through the use of weighted modeling as opposed to weighted averaging. Instead of convoluting data, we center a third-order 2D polynomial model on the pixel of interest and fit it to the local data using a weighting function (see Figure 3).

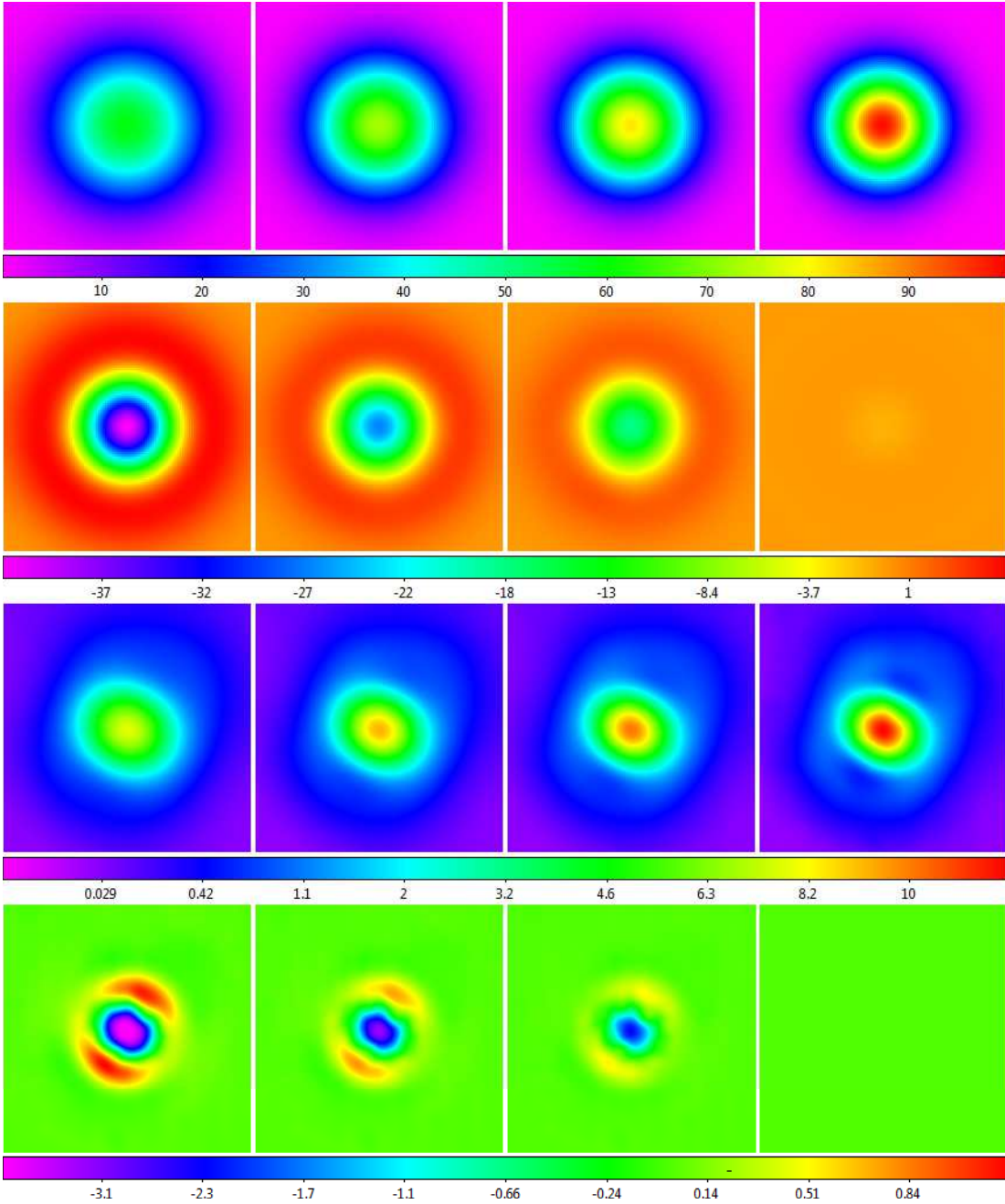


FIG. 3.— **First Row:** Simulated Gaussian point source sampled on a 1/5-beamwidth grid signal modeled using, from left to right: 1-beamwidth weighted averaging, 2/3-beamwidth weighted averaging, 1/2-beamwidth weighted averaging, and weighted modeling, as described in §2.6. **Second Row:** Residual error of each technique. **Third Row:** Cassiopeia A observed with one of the 20-meter's L-band unfocused linear polarization channels using a 1/5-beamwidth raster. Weighted averaging fails to recover the telescope's unfocused beam pattern, which is structured. **Fourth Row:** Difference between each of these techniques and weighted modeling. Square-root and squared scalings are used in the third and fourth rows to emphasize fainter structure (units are dimensionless, with one corresponding to the noise diode; see §2.1.)

So long as the model is sufficiently flexible to model the source and there is sufficient data to constrain, if not over-constrain the model, the signal can be recoverable at any location without blurring. The approach is outlined in §2.6 which demonstrates its ability to resolve simulated data with less than 1% error near the center of the beam pattern.

In addition to our decision to model, rather than average, data, we have also constructed our algorithm to do all contaminant cleaning before surface modeling—

whereas regridding techniques require cleaning to be done after signal modeling to accommodate techniques like frequency clipping within a 2D fourier transform.

### 1.3. Contamination Types

There are three primary types of radio contamination which our algorithm seeks to remove: en-route drift, radio frequency interference (RFI), and elevation dependent signal (each of which can be seen in Figure 5). En-route drift encompasses a broad set of contaminants that

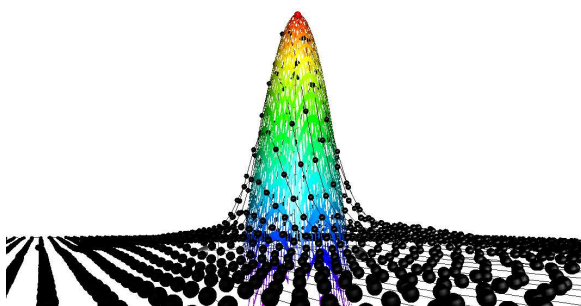


FIG. 4.— Weighted modeling of 20-meter data from the third row of Figure 3, at two representative points. Modeled surfaces span two beamwidths, but are most strongly weighted to fit the data over only the central, typically, 1/3 – 2/3 beamwidths, as described in §2.6. Only the central point (red) is retained.

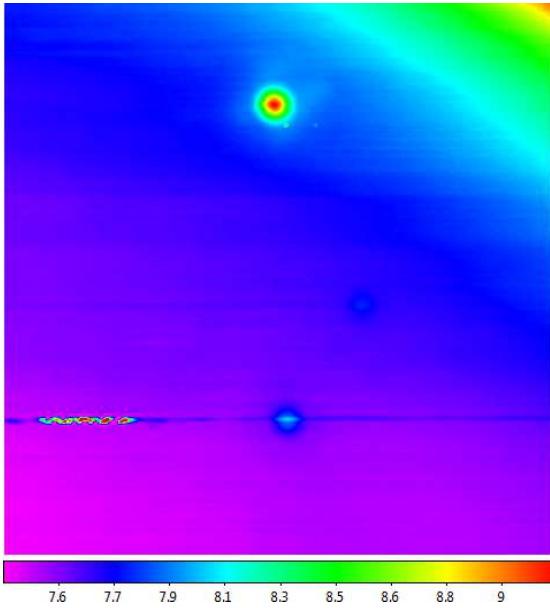


FIG. 5.— Raw map of Virgo A, 3C 270, and 3C 273—top, middle right, and bottom, respectively—acquired with a 1/10-beamwidth raster from the 20-meter in L band. The asymmetric beam pattern characterized in Figure 3 is partially corrected because the left and right channels have been combined prior to surface modeling. Locally modeled surface (§1.2, see §2.6) has been applied for visualization only. Major signal contaminants (§1.3) are present throughout the image: En-route drift is seen as the low-level variations along the horizontal scans, RFI is visible during the scan that passes through 3C 273 and near Virgo A, and elevation-dependent signal becomes pronounced toward the upper right ( $\approx 11^\circ$  above the horizon).

have collectively been referred to as the "scanning effect". These include 1/f noise, pink noise, and environmental variations in the atmosphere or spillover when the telescope points too close to the ground. These low-level contaminants are most noticeable scan-to-scan and can be made to vary over longer or shorter angular distances by moving the telescope faster or slower.

Sofue & Reich (1979) attempt to eliminate en-route drift by first isolating the en-route drift through unsharp masking and then modeling the drift using a second-order polynomial while using sigma clipping to extract only the small-scale structure from the scan. The faults in these procedures, however, are (1) that low-order polynomials may be inadequate when modeling en-route drift over large angular scales, (2) unmasking requires the blurring of data, a disadvantage we are seeking to avoid, and

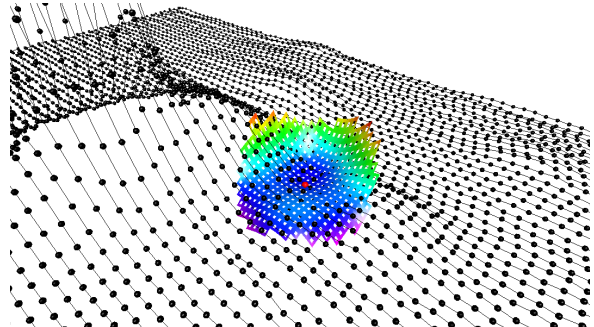


FIG. 6.— Green Bank Observatory 40-foot diameter radio telescope. (Photo credit: GBO)

(3) sigma clipping is a non-robust outlier detection algorithm.

Emerson & Grave Fourier transform the data and mask near-zero frequencies that contain the en-route drift. Ideally, this procedure is conducted when there are two maps with scans in orthogonal directions each transformed such that the real spacial frequencies can be retained. While this method does not assume that en-route drift can be modeled with a simple low-order function, it does unfortunately require that data be processed on a grid, and for best effects, requires that two orthonormal surveys be collected for the most accurate processing. Furthermore, this technique is not generalizable for non-rectangular mapping patterns, eliminating the possibility to remove the drift from daisies and noddings.

RFI is often localized to particular frequencies which, if known beforehand, can be masked prior to mapping. Triggered by events ranging from lightning strikes, radio-tracking devices, spark-plug engine cars, etc. RFI is one of the primary reasons radio telescopes are often constructed in particularly remote locations. In some cases, RFI can be spectrally non-local, appearing in continuum maps. These spectrally non-local events are, however, localized temporally, which can be used as a tool for identifying, isolating, and removing the contam-

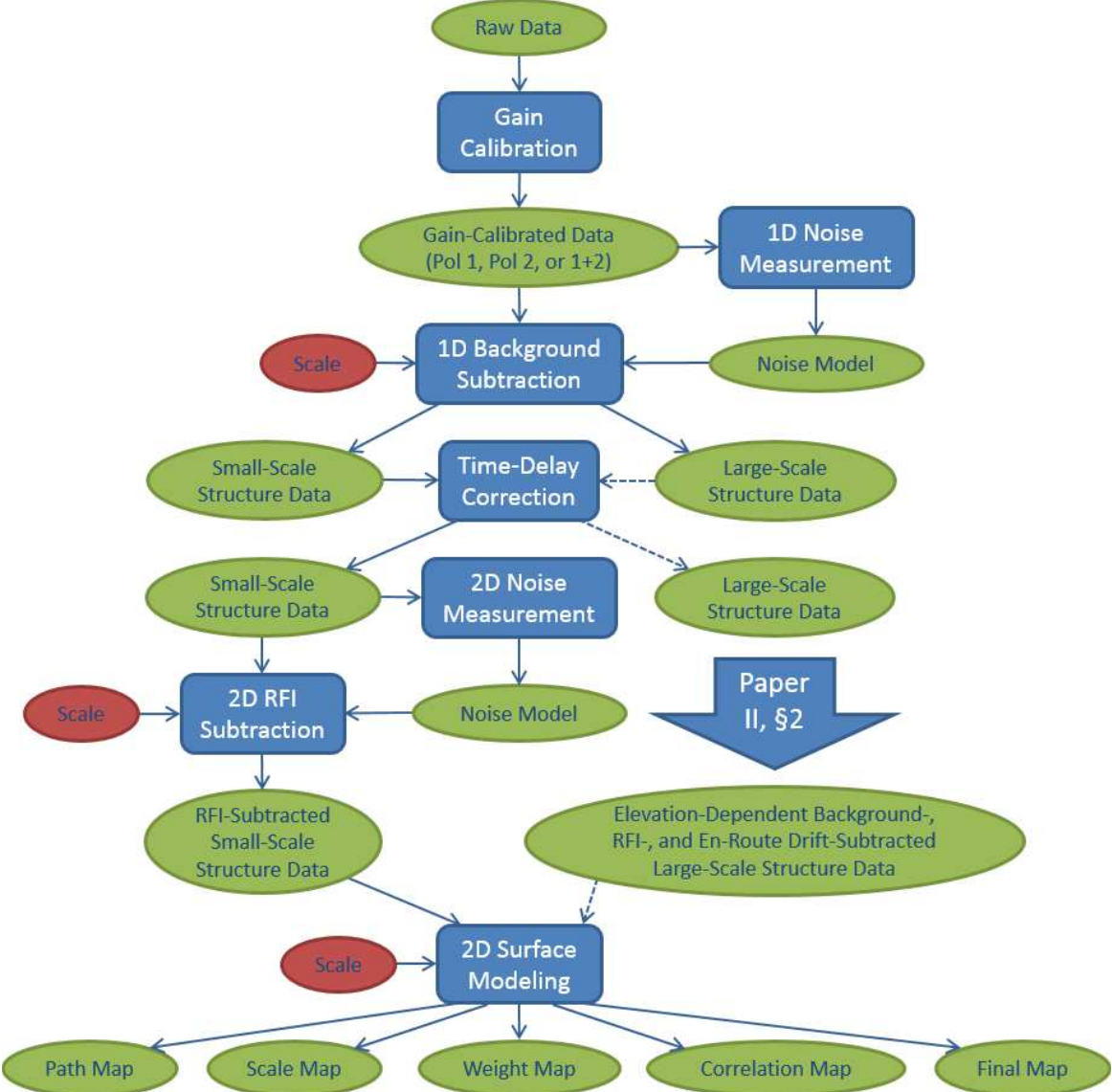


FIG. 7.— Flowchart of our algorithm for contaminant-cleaning and mapping small-scale structures. Blue boxes represent the internal algorithms, green ovals are the I/O of the corresponding algorithms, particularly the raw data, noise models, and maps. Red ovals are user-chosen parameters useful for isolating wanted and unwanted structures as well as final mapping.

inant. Given that temporarily local RFI does not exceed a beamwidth in scale, and moreover does not extend into multiple scans, it is possible to model data over the characteristic beamwidth scale in a 2D space and isolate the contaminant.

Elevation dependent signal occurs when the telescope slews close enough to the ground that terrestrial signal begins to spill into the antenna. Often this signal gets disguised in en-route drift, but it becomes apparent at high elevations.

Despite the differing modes of contaminant production, our algorithm models all of these contaminants the same way. By locally modeling the data with second-order polynomials, and using a robust form of outlier rejection to eliminate inaccurate local model values, our algorithm is capable of constructing a global model for each data point free of contamination.

#### 1.4. Robust Chauvenet Rejection

Sigma clipping is one of the simplest forms of outlier rejection; however, it is also one of the crudest. To use sigma clipping, scientists have the flexibility to determine how many sigma to consider characteristic of a distribution before excising them from the data set—a highly non-statistical procedure. One of the more popular attempts to remove this user-dependent ambiguity is Chauvenet's rejection, which is sigma clipping plus a reasonable rejection criteria:

$$NP(>|z|) = 0.5, \quad (1)$$

where  $N$  is the total number of data points and  $P(>|z|)$  is the cumulative probability of being more than  $z$  standard deviations from the mean, assuming a Gaussian distribution (Chauvenet 1863). Chauvenet rejection, however, also fails to resolve ambiguity because it relies on the mean and standard deviation of the data set which, if not known prior to measurement, are susceptible to the very outliers they are trying to reject, particularly in highly

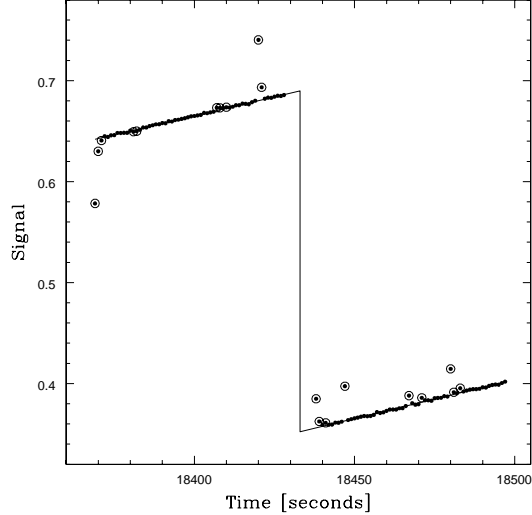


FIG. 8.— 40-foot gain calibration data, with the noise diode first on and then off, and best-fit model. Circled points have been robust-Chauvenet rejected, including data taken during the transitions from off to on and on to off, and RFI-contaminated data. The background level increased during the calibration, but our model accounts for this: Simply averaging each level, instead of modeling each level with a line, would have underestimated the result.

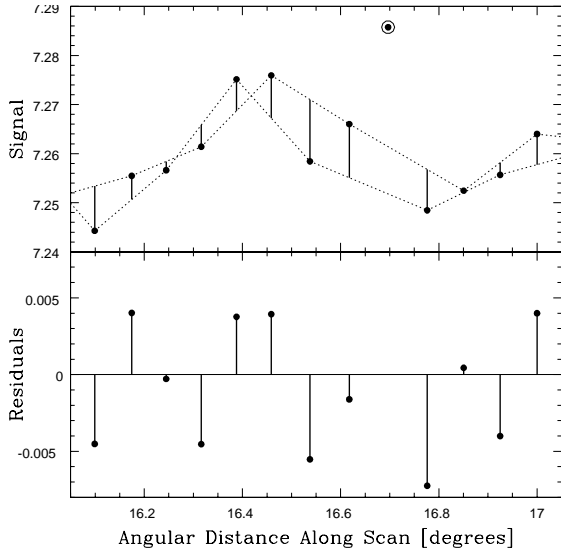


FIG. 9.— Point-to-point noise measurement technique. **Top:** The technique used for gain-calibrated 20-meter data—circled points were robust-Chauvenet rejected. **Bottom:** Deviations. Mean and standard deviations are measured from the non-rejected points, for each scan.

contaminated distributions. We have developed a new form of outlier rejection called robust Chauvenet rejection (Maples et. al. 2017) which resolves this ambiguity through the use of more robust measures of central tendency including mode, median, and the 68%-percentile deviation in an iterative fashion to remove the most extreme outliers before using more precise metrics such as the mean. This technique is used frequently throughout this paper, serving as a field-test to the integrity of the algorithm.

## 2. SOFTWARE

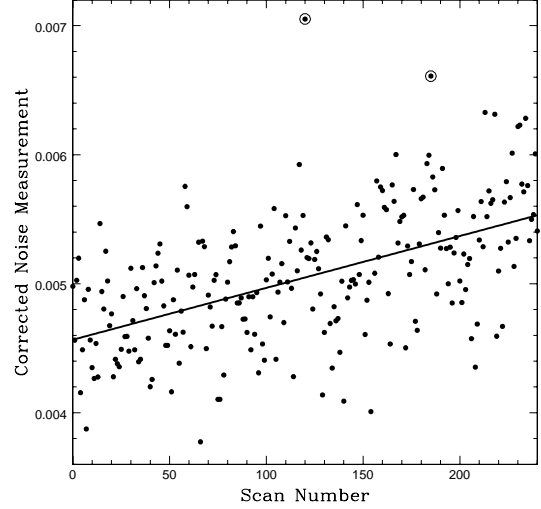


FIG. 10.— Corrected 1D noise measurements vs. scan number for a 20-meter observation, and best-fit model. Only two points met the robust Chauvenet rejection criterion, and then only barely, which is not unusual given that intra-scan outliers have already been rejected (Figure 9). The 1D noise level increased by  $\approx 20\%$  over the course of this observation.

In this section we outline the set of algorithms created to contaminant clean and map small-scale astrophysical structure (Figure 7). In §2.1 we calibrate the telescope against often small, variations in gain. In §2.2 we measure the point-to-point variation in signal which can be used to understand the characteristic noise of the data along a particular scan. In §2.3 we separate small-scale astronomical structure from both long- and short-duration RFI (including en-route drift, elevation signal, and large scale structure). In §2.4, we cross-correlate our scans to account for any time delay effect between the coordinate and signal device. In §2.5 we measure the noise differences between scans as a metric to further isolate instances of short-duration RFI from data points near the signal. In §2.6 we detail our surface modeling algorithm’s ability to interpolate data without blurring it beyond the instrument’s resolution. Finally, in §2.7 we outline the various image data products produced for the user.

### 2.1. Gain Calibration

Signal measurements in radio telescopes are calibrated against a noise diode. Ideally this is done when the telescope tracks the same point across the sky to minimize the amount of interference in the measurements. These measurements, however, are imperfect and are susceptible to extraneous noise as well as sensitivity to the diode transitioning between on and off. Consequently, we use RCR to reject the anomalous data and then we fit a line for both the diode being on and the diode being off. The difference between these two lines,  $\Delta$ , is what is used to calibrate the data (Figure 8).

Given that the 40-foot telescope<sup>3</sup> and the 20-meter telescope do not vary substantially over the time scale

<sup>3</sup> Skynet also makes use of data collected by the 40-foot educational radio telescope at Green Bank Observatory to verify the cross-compatibility of our algorithm with all single-dish radio telescopes.

TABLE 1  
MINIMUM RECOMMENDED 1D  
BACKGROUND-SUBTRACTION SCALE  
FOR THE TELESCOPES AND  
RECEIVERS OF §2, IN THEORETICAL  
BEAMWIDTHS

Telescope	Receiver	Scale
20-meter	L (HI + OH) <sup>a</sup>	7 <sup>c</sup>
20-meter	L (HI) <sup>b</sup>	6 <sup>c</sup>
20-meter	L (OH) <sup>b</sup>	6 <sup>c</sup>
20-meter	X	6 <sup>c</sup>
40-foot	L (HI)	3

<sup>a</sup> Before August 1, 2014

<sup>b</sup> After August 1, 2014

<sup>c</sup> The 20-meter’s beam pattern has a low-level, broad component, in both L and X bands, and consequently, we recommend larger background-subtraction scales here. This component was significant in L band prior to 8/1/14, as can be seen in the third row of Figure 3, as well as in Figure 5. Post 8/1/14, it was significantly reduced, but not altogether eliminated. This component corresponds to approximately 2% – 3% and 4% – 5% of the integrated beam pattern in L and X band, respectively. If this is not a concern, these minimum recommended 1D background-subtraction scales can be lowered to 3 and 4 theoretical beamwidths, respectively.

of the observation, we choose to calibrate only at the beginning and end of the observation. We then allow the user to choose between using the calibration at the beginning  $\Delta_1$ , end  $\Delta_2$ , or a linear interpolation between the two:

$$\Delta(t) = \Delta_1 + (\Delta_2 - \Delta_1) \frac{t - t_1}{t_2 - t_1}. \quad (2)$$

We calibrate each polarization channel individually and the user can choose to continue using either channel or a composite channel that sums the fluxes of both.

## 2.2. 1-D Noise Measurement

Here we measure the standard deviation of data on the most fundamental object type, the scan. For each data point within the scan, we fit a line to the two nearest non-rejected data points, and measure the deviation of the central point off of that line (Figure 9). Once a collection of these deviations are collected, we use RCR to extract the average deviation value, which tends towards zero, and its standard deviation which we then use as the noise model for the scan. We also allow for the noise value to change over time, so once all individual scan’s noise model has been constructed, we fit a line to their standard deviations using RCR to model the change in noise over time (Figure 10). This prevents scans that have excessive RFI from producing an uncharacteristically high noise value for a temporally anomalous set of events. The final value is the noise model for each signal measurement within that scan.

## 2.3. Background Subtraction

The majority of contaminants in radio data occur at the background level. Flux measurements can be biased

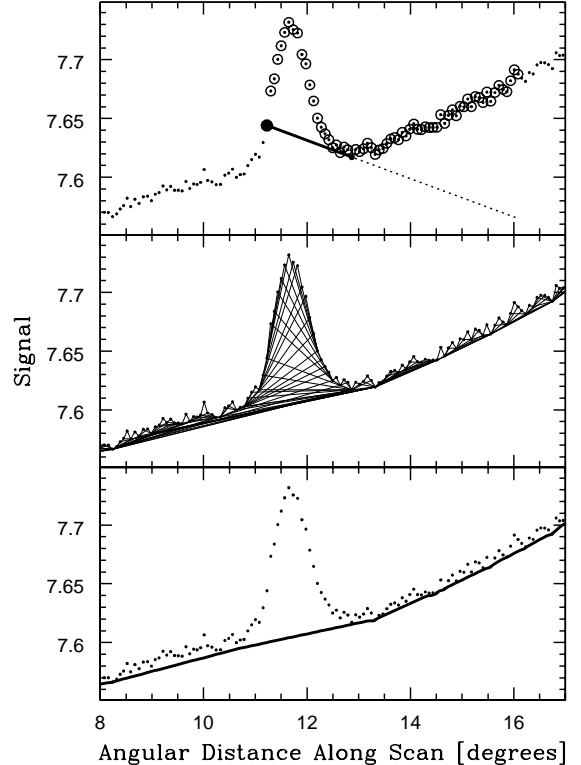


FIG. 11.— **Top:** A local background model applied in the forward direction and anchored to an arbitrary point from Figure 5, near 3C 270. Circled points indicate data that are within one background-subtraction scale length, but that still remain above the model. **Middle:** Forward- and backward-directed local background models, anchored to every point in the scan. **Bottom:** Global background model, constructed as a non-linear combination of lowest local background models.

by the dish pointing too close to the horizon causing the earth’s own radio emission to interlace with the astrophysical data. Features of long-duration RFI can corrupt a broad region of data points between one or more scans. Atmospheric variation and large-scale astrophysical structure can overlap with the small-scale structure source. To distinguish these deviant features from the small-scale sources, traditional algorithms fit lines between each point to every other point, and maintain only those that have all data between them above the line. This results in a global background model that falls entirely beneath the data, underestimating the background contamination given its extreme sensitivity to radio noise in the negative direction (Figure 11).

To distinguish between astrophysical sources and background contaminants, our algorithm instead models data locally over a user-defined scale. At each point, the algorithm collects all data within the user-defined scale and in the same scan. It then fits a quadratic regression model to the data (as opposed to linear which is often too inflexible to model contaminants), and calculates the total deviation of the collected data from the model. If the deviation exceeds the characteristic noise of the scan (as determined in §2.2), the most deviant point off of the model is removed, and the model is refit<sup>4</sup>. This cycle is

<sup>4</sup> To ensure the model does not underestimate the background model, our algorithm anchors to the original data point until the deviation of the data off of the model falls within the expected

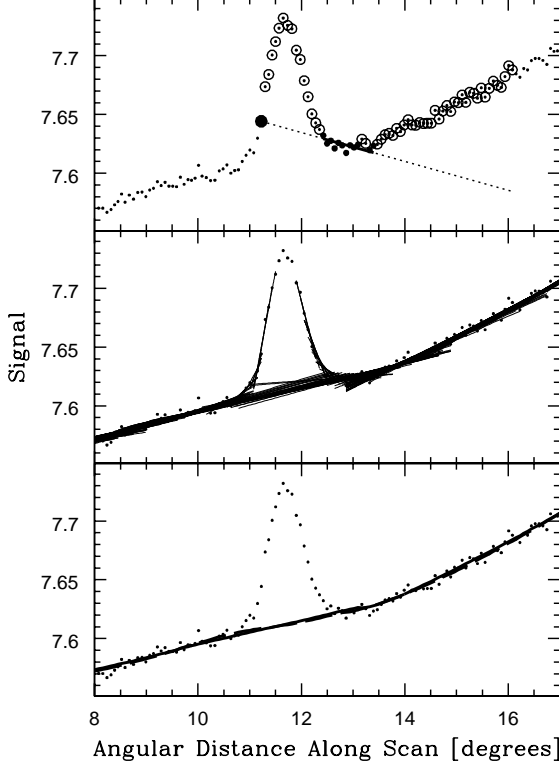


FIG. 12.— **Top:** A preliminary local background model, anchored to the same point as in Figure 11. Circled points have been iteratively rejected as too high, given the modeled noise level (§2.2); the larger points were not rejected. **Middle:** Final local background models once the original point is unanchored and is free to be rejected. **Bottom:** Global background model, constructed from the final local background models.

iterated through until the total deviation off of the model is less than the scatter within the original data.<sup>5</sup> These models will be fit through each data point, and once the model falls within the scatter of the scan, the resulting values of the model at each of the data points' location will be saved.

Once complete, each datum will contain a distribution of local-model values from these background fits, from which RCR can extract an accurate and precise global-model for the background flux at that point. We use weights that strengthen models that are produced near the center of the data, as their regression is more likely to be a more appropriate fit than unbound tales:

$$w_{ij} = \frac{\sum_j N_{ij}}{1 + \left( \frac{x_{ij} - \mu_i}{\sigma_i} \right)^2 + \delta \left( \frac{x_{ij} - \mu_i}{\kappa_i} \right)^4}, \quad (3)$$

where  $\sum_j N_{ij}$  is the number of non-rejected dumps that contributed to the  $i$ th local background model,  $w_{ij}$  is the weight of the  $j$ th point from the  $i$ th local background model,  $x_{ij}$  is the angular distance of this point along the scan,  $\mu_i$  is the dump-weighted mean angular distance of

value. At this point, we unanchor this point and allow the model to be refit and iteratively allow points back in to ensure there was not an overrejection of data. This allows the global model to fit within the noise level of the data rather than under it (Figure 12)

<sup>5</sup> If the algorithm continues to reject data such that there is no longer sufficient data to model a quadratic regression, the algorithm will attempt a linear fit and repeat this procedure.

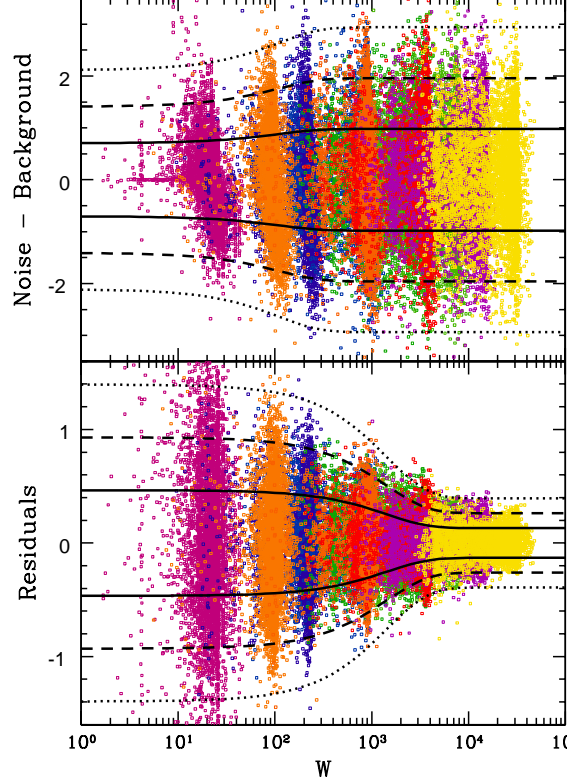


FIG. 13.— Gaussian random noise background-subtracted (top) and residuals (bottom) vs.  $W$ , the sum of the weights of the non-rejected local background models that determine the global background model at each point, for 1/10- and 1/5-beamwidth rasters, and for 1-, 3-, 6-, 12-, and 24-beamwidth background-subtraction scales (background-subtraction scale times sampling density of the data sets increases from left to right). The RMS of the data varies with  $W$ , but not with background-subtraction scale or sampling density independently. Curves are 1-, 2-, and 3- $\sigma$  model noise envelopes that have been fitted to all of these data simultaneously (Equations 6 and 7).

all of the non-rejected points from the  $i$ th local background model,  $\sigma_i$  is the dump-weighted standard deviation of these values,  $\kappa_i$  is analogous to standard deviation, and is related to these values' kurtosis:

$$\kappa_i = \left[ \frac{\sum_j N_{ij} (x_{ij} - \mu_i)^4}{\sum_j N_{ij}} \right]^{1/4}, \quad (4)$$

and  $\delta$  is zero for linear local background models and one for quadratic local background models (analogous terms can be added for higher-order local background models). Once calculated, the user has a global background model which can be subtracted off of the original data to remove long-duration RFI, elevation dependence, enroute drift, and underlying large-scale structure.

### 2.3.1. Background Subtraction Verification

To test the validity of this procedure, we designed a simulated data set that layers increasingly prominent and complex containment types.<sup>6</sup> The first layer includes a standard gaussian noise model across the image. We apply our background subtraction procedure using 6-, 12-, and 24-beamwidth scale and evaluate its

<sup>6</sup> These images and their residuals appear in Appendix A.

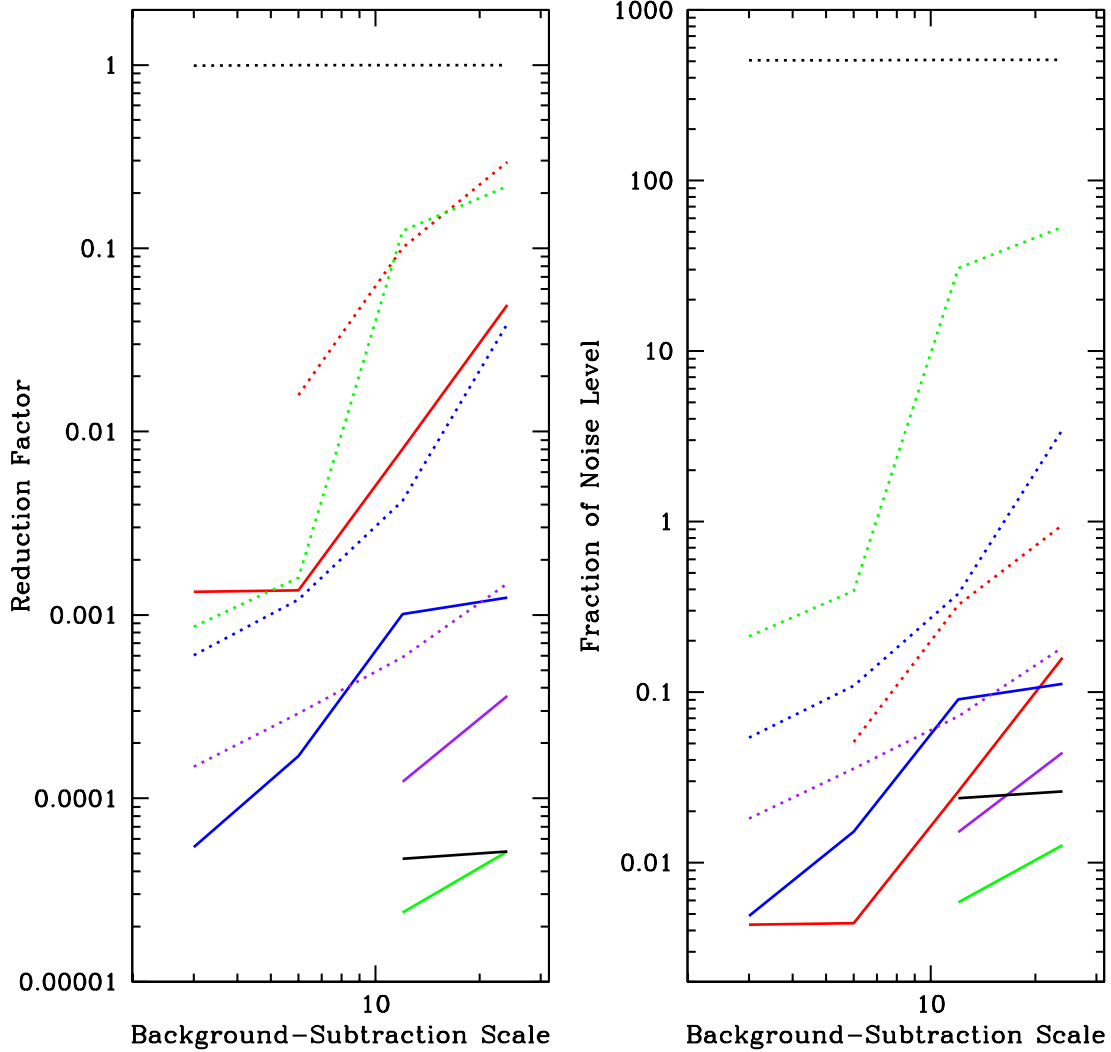


FIG. 14.— **Left:** Factor by which background subtraction reduces en-route drift (red), long-duration RFI (green), large-scale astronomical signal (blue), elevation-dependent signal (purple), and short-duration RFI (black) in our simulated data, for background subtraction scales of 3, 6, 12, and 24 beamwidths (dashed curves). Factor by which background and RFI subtraction (see §2.5) reduce these contaminants (solid curves). **Right:** Fraction of the noise level to which these contaminants are reduced. If nothing is plotted, the contaminant was simulated separately, and in the absence of sources.

performance by measuring the residual off of the uncontaminated values (Figures A.1 and A.2). We find that the background subtracted data are neither biased high or low and the noise level is nearly identical to that of the original data. Furthermore, the RMS of the residuals is much less than the original data. These quantities are determined by the number of local models to the point  $j$ 's global models, as well as their collective weights. For example, for smaller background scales or closer to the edge of the scan where fewer data are collected, the greater the residual RMS values. These residuals are plotted against the summed weight,  $W$ , of all local models in Figure 13 where

$$W = \sum_i w_{ij}. \quad (5)$$

We supplement this data using 1- and 3-beamwidth background scales and find that the noise level of the background-subtracted data is well-modeled by:

$$\sigma_1 \approx 0.979 - 0.275e^{-W/109} \quad (6)$$

and that the RMS of the residuals is well-modeled by:

$$\sigma_2 \approx 0.131 + 0.334e^{-W/1415}, \quad (7)$$

relatively independent of background subtraction scale and sampling density. The fact that the noise level of the background-subtracted data is less than the original data is because some of the variability is getting caught by the subtraction routine, though for high values of  $W$  it returns to the original values. Likewise, the RMS of the residuals decreases as more information is incorporated, but only to a limit. Finally  $\sigma_1^2 + \sigma_2^2 \approx 1$  for all values

of  $W$  suggesting that no additional variability is being included through the routine itself.

In conclusion, background subtraction errors in the absence of small- or large-scale data by a factor as high as  $\approx 47\%$  of the original noise for small  $W$  values to as low as  $\approx 13\%$  for large values of  $W$ . Furthermore, these are random errors biasing the data equally in the positive and negative directions, reducing the noise of the data by  $\approx 30\%$  for very small values of  $W$  to only  $\approx 2\%$  for large values of  $W$ .

Next we add simulated gaussian point sources to our image as well as short duration RFI (Figure A.3). We again background subtract with scales of 6-, 12-, and 24- beamwidths, and extract their residuals (Figure A.4). We find three underlying causes of the residuals. The first is an underestimation directly underneath the source, however it is independent of the brightness of the source. The bias level is best defined by

$$\text{peak bias level} \approx -\frac{(0.5 - 1) \times \text{noise level}}{\left(\frac{\text{background subtraction scale}}{6 \text{ beamwidths}}\right)}. \quad (8)$$

which is at a sufficiently low level that it can be ignored. Furthermore, when the sources are replaced with cosine functions with less winged tails, the factor decreases by a factor between 2 and 3. These systematic biases are further corrected by our RFI-subtraction algorithm (§2.5) in regions near the sources.

The second bias is attributed to sources that are close in proximity as collectively they can exceed the length of the original background subtraction scale. These effects are best mitigated by use of larger background-scales such as 12- and 24-beamwidths.

The final bias occurs when a source lay within 1- to 2-beamwidths of the edge of the survey—an area where the background model no longer has sufficient data to constrain its regression. This is a known deficiency in our algorithm, but it is local and easy to define allowing us to give the user the option to clip these data before surface-modeling if desired.

Next in our simulated image we include en-route drift and long-duration RFI (Figure A.5). Like the gaussian noise and the point sources, we model these data using a 6-, 12-, and 24-beamwidth scale and measure the residuals (Figure A.6). We find that the background subtraction routine is effective at reducing the effects of the contaminants given that the background-scale is sufficiently below the scale of the large-scale structure (12-beamwidths in this simulation). We find that en-route drift and long-duration RFI are reduced by factors of  $\approx 3$  and  $\approx 5$ , to  $\approx 96\%$  of and  $\approx 53$  times the noise level, respectively, when background-subtracted on double this scale (24-beamwidths); by factors of  $\approx 63$  and  $\approx 630$ , to  $\approx 5\%$  and  $\approx 39\%$  of the noise level, respectively, when background-subtracted on half of this scale (6-beamwidths); and by even greater factors when background-subtracted on even smaller scales (see Figure 14). These gains are significantly furthered by our RFI-subtraction algorithm.

Lastly we include 2D large-scale structure and find that the results are closely paralleled to that of long-duration RFI and en-route drift (Figure A.7). We find that large-scale astronomical and elevation-dependent signal is reduced by factors of  $\approx 26$  and  $\approx 670$ , to  $\approx 3$  times and

$\approx 18\%$  of the noise level, respectively, when background-subtracted on the scale of the map (24 beamwidths); by factors of  $\approx 830$  and  $\approx 3400$ , to  $\approx 11\%$  and  $\approx 4\%$  of the noise level, respectively, when background-subtracted on the 6-beamwidth scale; and by even greater factors when background-subtracted on even smaller scales (Figure A.8).

### 2.3.2. 20-Meter and 40-Foot Data

After verifying functionality of background subtraction on simulated data, we proceed to test its functionality on real data from the 20-meter and 40-foot telescopes. We demonstrate its function on a 20-meter L-band raster of Virgo using both small and large background-subtraction scales (Figure 15), two heavily contaminated maps of Andromeda (Figure 16), a daisy map of 3C 84 taken with the 20-meter in X Band to demonstrate its application on non-rectangular mapping patterns (Figure 17), and finally two nodding maps of the sun using the 40-foot (Figure 18).

### 2.4. Time-Delay Correction

In the case of the 20-meter telescope, the signal is integrated over a user-defined time, and coordinate information is recorded at the midpoint of this integration time. However, with the 40-foot, signal is run through an RC filter, with a user-defined time constant, typically 0.1 seconds, but signal and coordinate values are sampled simultaneously, resulting in an effective delay between the two due to the time constant (Figure 20). This results in alternating coordinate errors in alternating scans. Even with the 20-meter, the same can happen if the signal and coordinates computers' clocks become unsynchronized.

To correct for this, we cross-correlate adjacent scans. The position of the maximum value of the cross-correlation gives the best angular shift between the scans, and the square root of this value gives a weight. If the scans intersect a source, the best angular shift is well defined, and the weight is correspondingly high. If they intersect only noise, the best angular shift is not well defined and the weight is low. For all adjacent scans we measure the best angular shift and reject outliers using RCR and take the mean of the remaining values and divide by the telescopes slew speed to convert to time. We again perform RCR to eliminate periods of telescope acceleration (Figure 19). We then take the final time and interpolate the telescope's coordinate values accordingly.

### 2.5. RFI-Subtraction

Once long-duration contamination has been removed and the individual scans are aligned with one another, the algorithm proceeds to remove remaining RFI-contaminants. The procedure involves fitting a two-dimensional cosine to local data, and, in a manner similar to background subtraction, rejecting deviant points and remodeling the cosine until the total deviation between data and model falls within the characteristic noise (§2.5.1) of the survey.

#### 2.5.1. 2-D Noise Model

To properly remove RFI, we must first re-measure the standard deviation of the background subtracted data on the smallest scale available. We refer to this metric

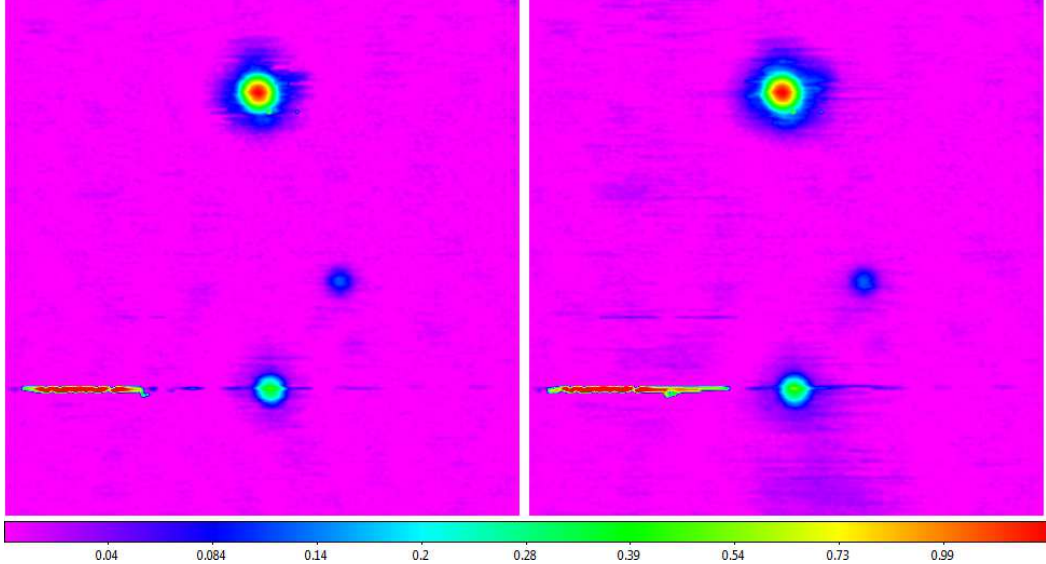


FIG. 15.— 20-meter L-band raster from Figure 15 background-subtracted, with 7- (left; Table 1) and 24- (right) beamwidth scales (the map is 24 beamwidths across). Locally modeled surfaces (§1.2, see §2.6) have been applied for visualization only. Hyperbolic-arcsine scaling is used to emphasize fainter structures.

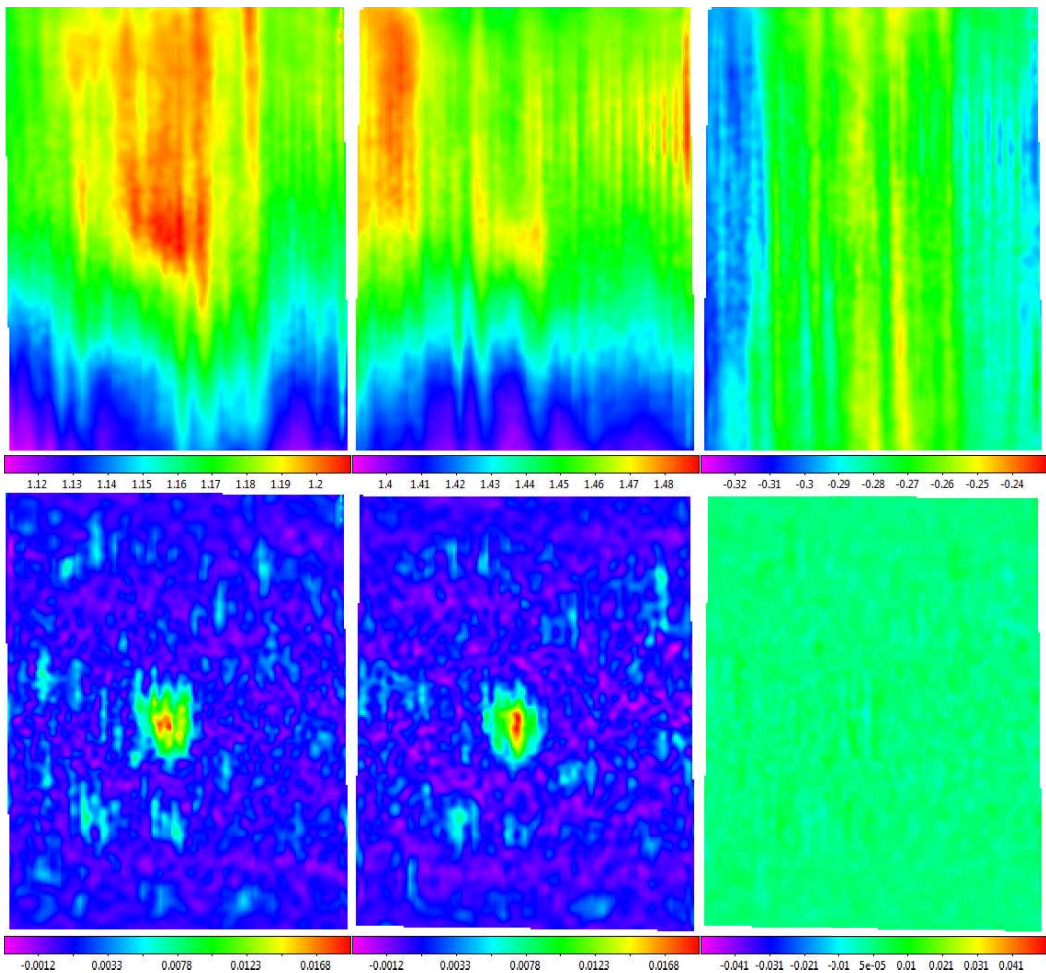


FIG. 16.— **Top Row:** The left and middle columns are raw maps of Andromeda post-time delay correction (§2.4), acquired with the 40-foot in L band. Contamination in the form of instrumental signal drift dominates each map. Their difference is plotted to the right. **Bottom Row:** Data from the top row background-subtracted (left and middle), with a 5-beamwidth scale (larger than the minimum recommended scale from Table 1, given the size of the source), and their difference (right, spanning the same scale range as above). Similar maps are extracted, despite the large systematics. Locally modeled surfaces (§1.2, see §2.6) have been applied for visualization only.

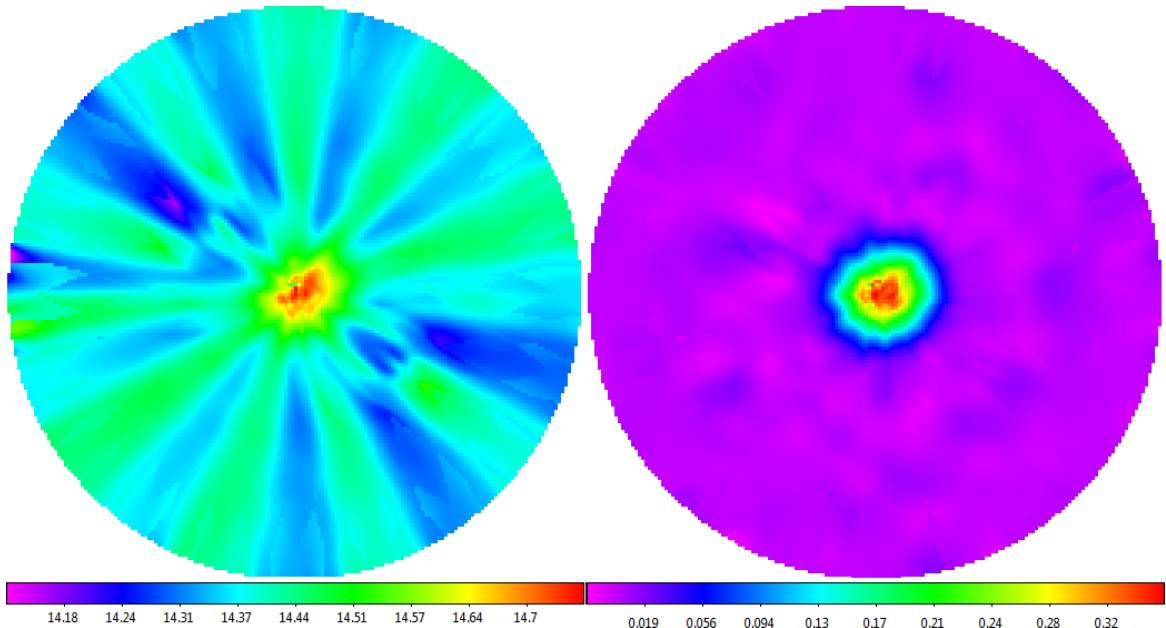


FIG. 17.— **Left:** Raw map of 3C 84, acquired with the 20-meter in X band using a 20-petal daisy pattern. **Right:** Data from the left panel background-subtracted, with a 6-beamwidth scale (Table 1). Locally modeled surfaces (§1.2, see §2.6) have been applied for visualization only.

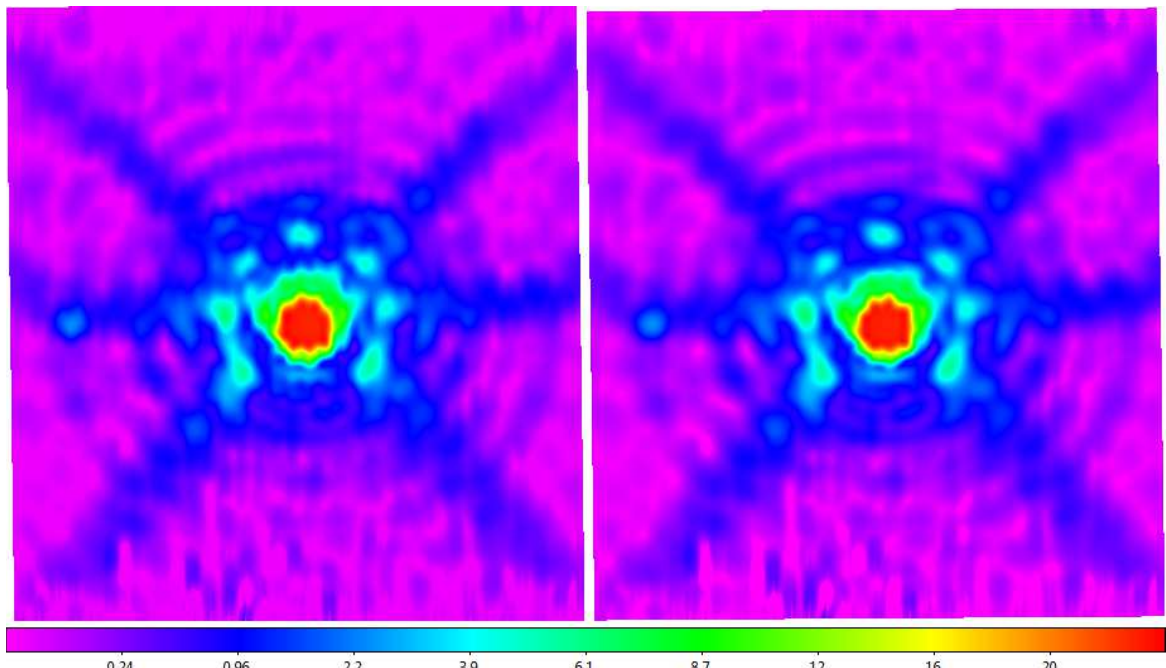


FIG. 18.— Background-subtracted map of the sun in L band, highlighting the 40-foot's diffraction pattern, before (left) and after (right) time-delay correction. The center is saturated. Taurus A is to the left. Locally modeled surfaces (§1.2, see §2.6) have been applied for visualization only. Square-root scaling is used to emphasize fainter structures.

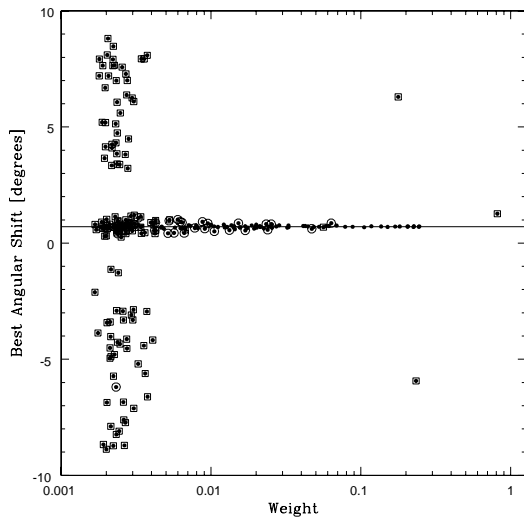


FIG. 19.— Best angular shift between adjacent scans vs. cross-correlation weight for all scans in a 20-meter observation. Many of the low-weight best angular shifts are not well defined, because their corresponding scans are noise-dominated. A few of the high-weight best angular shifts are incorrect, due to RFI contamination (consequently, simply taking the weighted mean of these values would yield a poor result). To eliminate both cases: For each best angular shift, we calculate the probability that it could, by chance alone, be as close as it is to both its preceding and proceeding values,<sup>a</sup> and eliminate all best angular shifts for which this probability exceeds one half divided by the best angular shift sample size (e.g., Chauvenet 1863, Maples et al. 2017; squared points). The remaining best angular shifts repeat consistently for at least three consecutive measurements, and consequently are likely due to astronomical signal, not noise or RFI contamination. We take the unweighted mean of these values (line), robust-Chauvenet rejecting any remaining outliers (circled points).<sup>b</sup>

<sup>a</sup>For two, adjacent, best angular shifts,  $\delta_i$  and  $\delta_{i+1}$ , it is not difficult to show that this probability is given by  $p_{i,i+1} = \frac{|\delta_{i+1}-\delta_i|}{\Delta} \left( 2 - \frac{|\delta_{i+1}-\delta_i|}{\Delta} \right)$ , where  $\Delta$  is the angular length of the scans. For three, this probability is given by  $2p_{i-1,i}p_{i,i+1}$ .

<sup>b</sup>We reject outliers as described in §8 – §10 of Maples et al. 2017, using iterative bulk rejection followed by iterative individual rejection (using the mode + broken-line deviation technique, followed by the median + 68.3%-value deviation technique, followed by the mean + standard deviation technique), using the smaller of the low and high one-sided deviation measurements. Data are weighted equally, in case any of the remaining high-weight data are still biased by RFI contamination (or by source saturation, as is the case in Figure 18).

as the 2-D noise, and its measurement includes taking each data point within a scan, identifying the closest datum in the proceeding and preceding scans, fitting a line to those two datum and then measuring the deviation of the original point from this line. Once all data deviations within the scan have been measured, RCR is then used to remove the most discrepant deviations and to extract the precise across-scan noise value for that scan. This is repeated for each scan within the survey. Once all scans have a characteristic two-dimensional noise value, a line is fit to these data across the scans on which RCR is again performed. This prevents scans contaminated by long-duration RFI to bias the characteristic noise of the larger survey (Figure 22). When fitting to uncontaminated gaussian data, we find this method overestimates the true noise value by 22.9%. We correct each scan’s noise value accordingly.

### 2.5.2. Cosine-fit

Similar to the procedure used in background subtraction, RFI-subtraction creates a collection of local models from which a global model of the non-contaminated data can be extracted. The primary difference between background subtraction and RFI-subtraction is that RFI-subtraction seeks to eliminate contaminants on a sub-beamwidth scale. While RFI can extend beyond the scale of the source in the direction of the scan, it is unlikely to repetitively continue through all pre- or proceeding scans such that it extends the beamwidth scale across scans. As such, we can strategically model our data in using a 2D-cosine to recover the astrophysical signal rather than the contaminant.

Specifically we use the two-parameter local model of

$$z(\Delta\theta) = \begin{cases} f \cos^2 \left( \frac{\pi \Delta\theta}{2\theta_{RFI}} \right) + z_0 & \text{if } \Delta\theta < \theta_{RFI} \\ 0 & \text{otherwise} \end{cases}, \quad (9)$$

where  $\Delta\theta$  is the 2D angular distance from the model’s center,  $\theta_{RFI}$  is a user-defined RFI-subtraction scale, and  $f$ , the first of the two fitted parameters, normalizes the function in the first term, and  $z_0$ , the other fitted parameter, adds a small, local, background value (Figure 23). This allows us to model a point source almost exactly when  $\theta_{RFI} \approx 1$  beamwidths, and if  $\theta_{RFI}$  is chosen to be slightly smaller than the true FWHM of the telescope’s beam pattern, it can be used to separate astrophysical signal from marginally sub-beamwidth structures.

This model is centered at each data point, and the algorithm proceeds to calculate the total deviation of all data from the model. If the deviation exceeds the anticipated two-dimensional noise value, it then proceeds to reject the most positive outlier if  $f > 0$  or the most discrepant outlier if  $f < 0$  and refit. The procedure continues on until the standard deviation of the non-rejected points is consistent with the noise model. The end product results in a singular local model, defined only at the non-rejected points (Figure 25). This procedure is repeated for all data within the survey, constructing a distribution of local models for each data point.

Once local models are constructed for each data point, the algorithm performs RCR on each datum’s local model distribution to construct the global model value. RCR’s output produces the RFI-cleaned data points which will be used for surface modeling (§2.6). All data that never earned a local model are assumed to be RFI and are excised from the data set.

In theory, the RFI-subtraction scale need be only slightly smaller than the FWHM of the beam pattern to successfully remove contaminants. However, in practice, the source may be more peaked than the model or asymmetric. In these cases, a smaller RFI-subtraction scale is recommended, but the user is cautioned to remain aware that smaller scales risk high rejection rates of data that is part of the astrophysical source (Figure 32). We present recommended RFI-subtraction scales for both the 20-meter and 40-foot telescopes in Table 2.

### 2.5.3. RFI-Subtraction Verification

To confirm the effectiveness of the our RFI-subtraction routine, we apply it to the same increasingly complex simulated data as in §2.3.2 (Figures A.1, A.3, A.5, A.7).

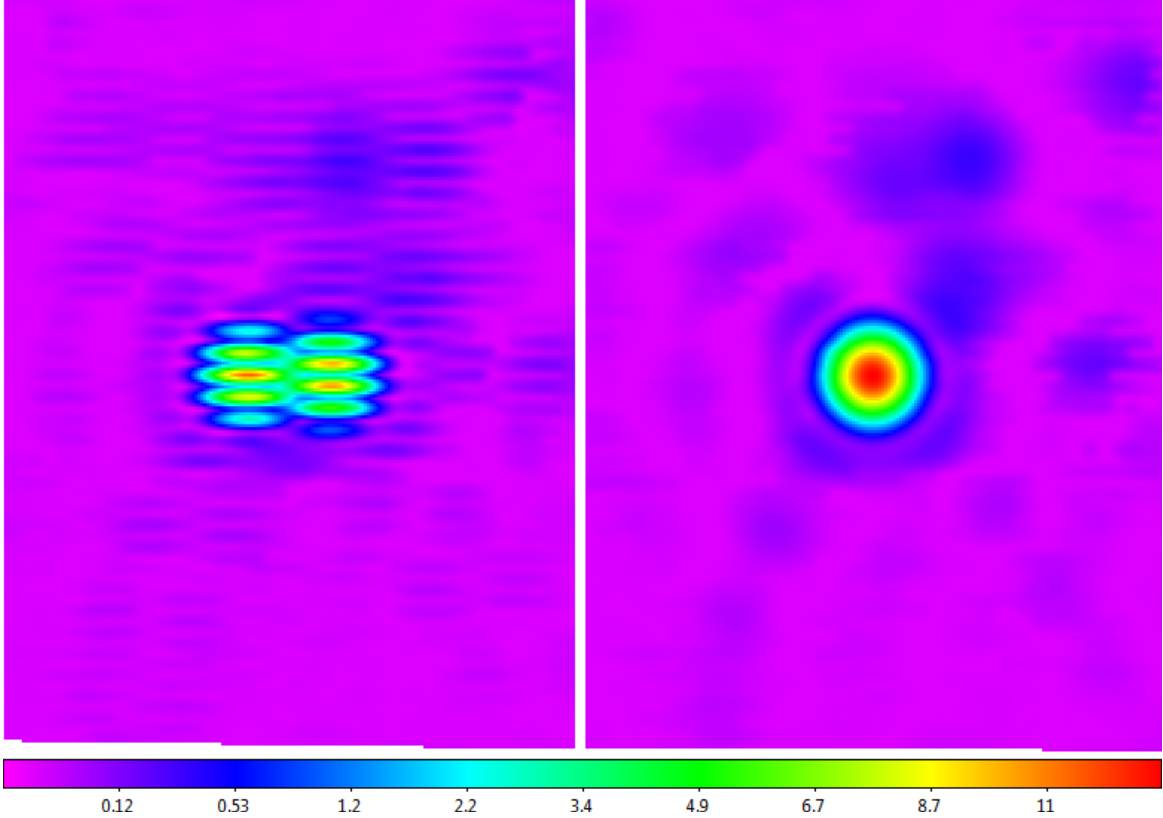


FIG. 20.— Background-subtracted map of Cassiopeia A in L band, acquired with the 20-meter with signal and position computers' clocks unsynchronized, before (left) and after (right) time-delay correction. Locally modeled surfaces (§1.2, see §2.6) have been applied for visualization only. Square-root scaling is used to emphasize fainter structures.

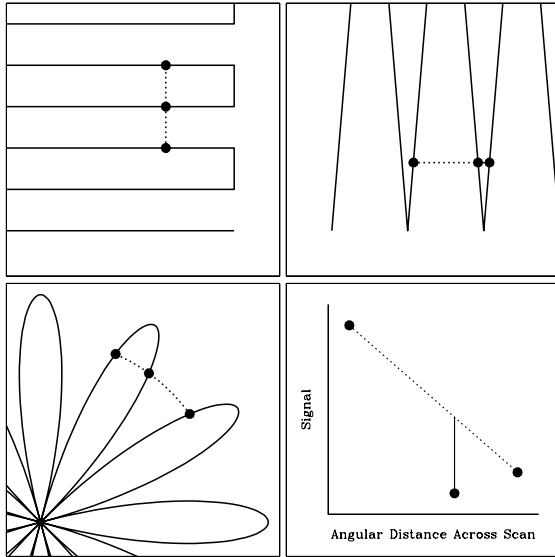


FIG. 21.— Scan-to-scan measurement technique as applied to the three primary mapping techniques. Residuals are measured (bottom right), and mean and standard deviations are measured from the non-rejected points, for each scan.

First we analyze the algorithm's performance on gaussian noise with a RFI-subtraction scale of 0.95 beamwidths as well as a RFI-subtraction scale of 0.5 beamwidths (Figure B.1). We find that the RFI-subtracted data are not biased high nor low and the noise level is significantly less than the original background-subtracted data. We then

TABLE 2  
MAXIMUM RECOMMENDED 2D RFI-SUBTRACTION SCALE FOR THE TELESCOPES AND RECEIVERS OF §2, IN THEORETICAL BEAMWIDTHS

Telescope	Receiver	Scale	
		Left or Right Channel	Left + Right Channel
20-meter	L (HI + OH) <sup>a</sup>	0.8	0.9
20-meter	L (HI) <sup>b</sup>	0.7	0.8
20-meter	L (OH) <sup>b</sup>	0.9	1.1
20-meter	X	0.8	0.8
40-foot	L (HI)	0.7	0.7

<sup>a</sup> Before August 1, 2014

<sup>b</sup> After August 1, 2014

add point sources and short-duration RFI to the simulated data and repeat the algorithm. We find that the short-duration RFI, which was only marginally reduced by background subtraction was reduced by a factor of  $\approx 19000$  to  $\approx 3\%$  of the noise level, when the background-subtraction scale was 24 beamwidths (Figure B.2). The signal of the RFI was further reduced to immeasurable levels when a background scale of 6-beamwidths was used. The residuals of the point sources were reduced to completely negligible levels beyond where the sources intersect the noise level, and increased only slightly at the boundaries. Otherwise the residuals remain consistent with the residuals measured after background subtraction. These factors are again reduced when the sources are replaced by more realistic, less-winged models.

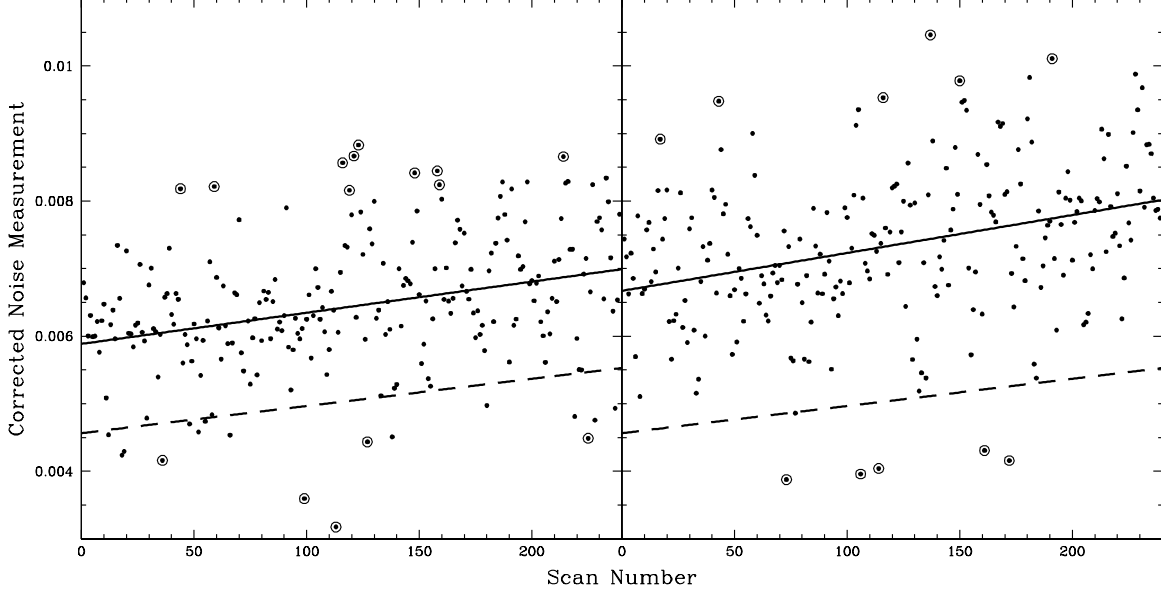


FIG. 22.— **Left:** Corrected 2D noise measurements vs. scan number for the 20-meter observation from Figure 10, after background-subtracting on a 6-beamwidth scale, and best-fit model (solid line). Circled points have been robust-Chauvenet rejected. 1D noise model from Figure 10 is included for comparison (dashed line). The 2D noise level is  $\approx 28\%$  higher, due to residual 1D structures (e.g., residual en-route drift) post-background subtraction. **Right:** Same, but with a 24-beamwidth background-subtraction scale. In this case, the 2D noise level is  $\approx 46\%$  higher than the 1D noise level, because contaminants are less completely eliminated on longer background-subtraction scales (e.g., Figure 14).

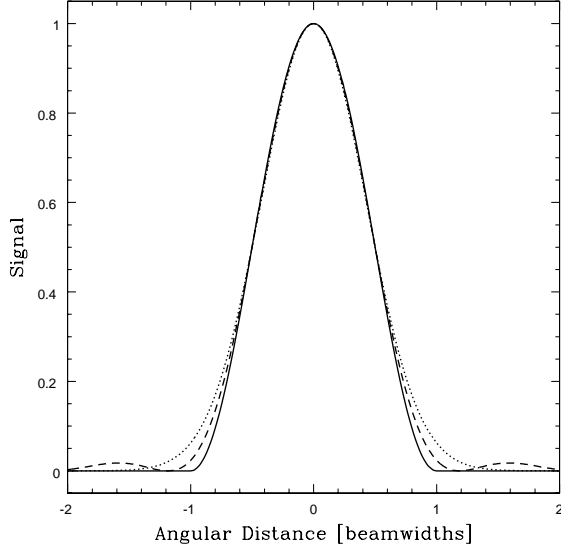


FIG. 23.— Local model (Equation 9) with  $\theta_{RFI} = 1$  beamwidth and  $z_0 = 0$  (solid curve), and Airy (dashed curve) and Gaussian (dotted curve) functions, each with FWHM = 1 beamwidth.

Next we include 1D large-scale structure contamination in the form of en-route drift and long-duration RFI. We find that long duration RFI is now reduced by a factor of  $\approx 19000$  to  $\approx 1\%$  of the noise level when the background-scale was 24-beamwidths (Figure B.3). The signal was further reduced when the background-scale approached 6-beamwidths. We also find that en-route drift is reduced by a combined factor of  $\approx 20$  to  $\approx 16\%$  of the noise level when background subtracted on the scale of the map; this factor increases to a factor of  $\approx 730$  or  $\approx 0.4\%$  of the noise level when background-subtracted on the 6-beamwidth background-subtraction scale. For reference, the basket-weaving technique of Winkel, Floer

& Krauss (2012) reduces en-route drift by a factor of  $\approx 10$  under ideal circumstances.

Finally, we include 2D large-scale structure contamination through the inclusion of elevation-dependant signal and background structure (Figure B.4). Away from the sources, we find that the elevation-dependent signal is reduced by a combined factor of  $\approx 2800$  or  $\approx 4\%$  of the noise level when background subtracted on the scale of the map (24-beamwidths). The signal is reduced to immeasurable levels when background subtracted on the 6-beamwidth scale. We find that the astronomical signal is reduced by a combined factor of  $\approx 800$  to  $\approx 11\%$  of the noise level when subtracted on the scale of the map, and to a factor of  $\approx 5900$  or  $\approx 2\%$  of the noise level when background-subtracted with a 6-beamwidth scale.

#### 2.5.4. RFI-Subtraction on Real Data

After verifying the effectiveness of RFI-subtraction on simulated data, we proceed to test its functionality on real data. First we use a wide-field survey with extreme amounts of RFI-contamination collected by the 40-foot telescope (Figure 26). The contamination was the result of a broadband emitter from the Roanoke, VA airport located 100 miles south of Green Bank. The signal is linearly polarized appearing in only one of the telescopes two channels. We find that after RFI-subtraction the contaminated and uncontaminated channels are nearly identical.

We also apply our RFI-subtraction procedure to Figure 16 and Figure 15 to produce Figures 27 and 30.

In addition to successful RFI-subtraction, our algorithm allows us to append images for additional local models and robustness particularly on low S/N sources and temporally localized contamination. By collecting data of the same part of the sky over multiple observations, fainter structure becomes more apparent, and any idiosyncratic contamination can be more effectively

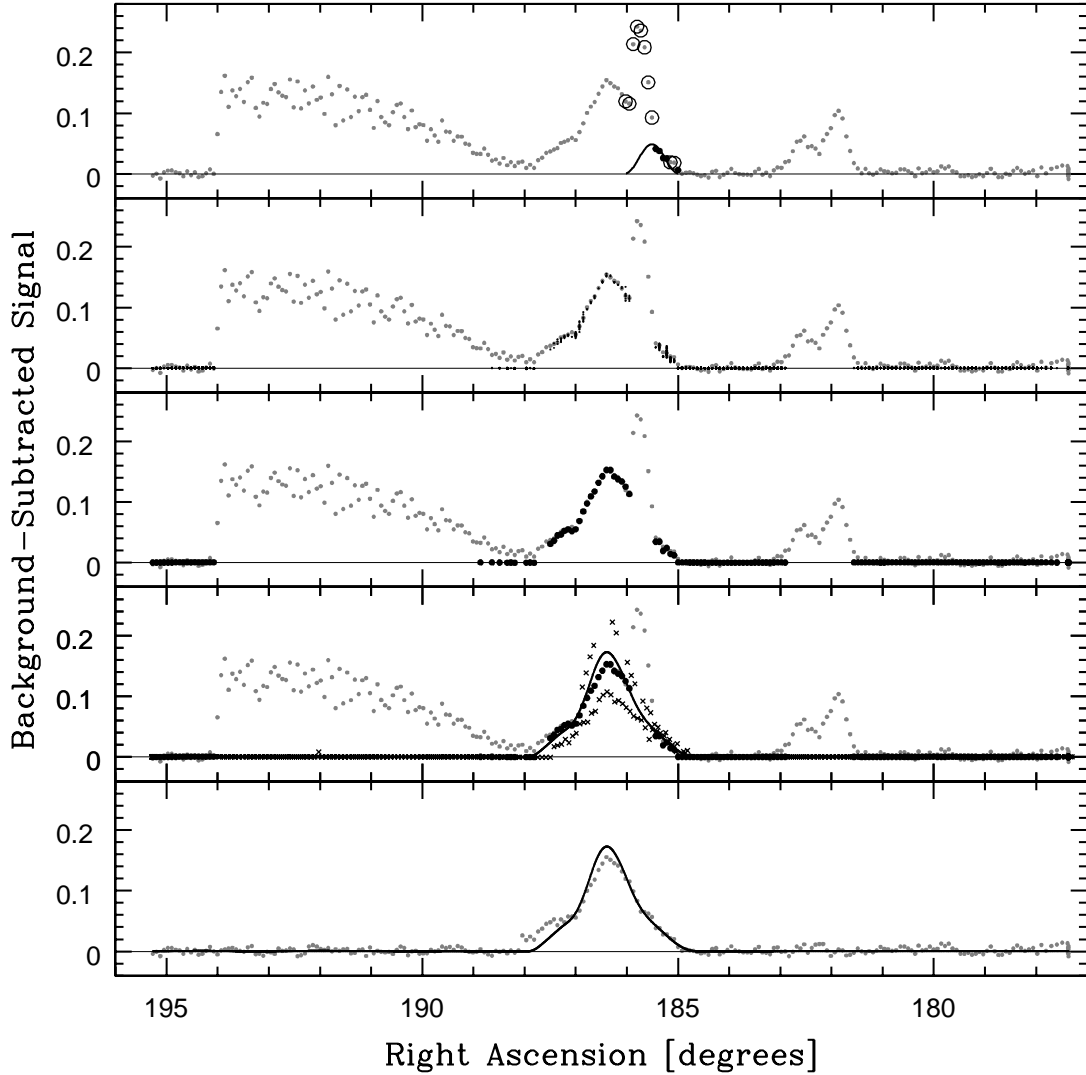


FIG. 24.— **First:** 1D cross-section along a scan that simultaneous visualizes a profile of a single 2D local model, centered on an arbitrary point from the left panel of Figure 15, near Virgo A (curve). We have contaminated this scan with three instances of simulated RFI (the original, uncontaminated data are plotted in the fifth panel). Circled points have been iteratively rejected as too high, given the modeled noise level (§2.5.1); the larger, darker points were not rejected. **Second:** Every local model that intersects this scan, evaluated at each local model’s non-rejected points (smaller, darker points). All simulated RFI has been rejected, being too narrow—as compared to the RFI-subtraction scale ( $\theta_{RFI} = 0.9$  beamwidths; Table 2)—either along or across the surrounding scans. **Third:** Global model (larger, darker points), produced via RCR on the distributions of local models at each point. **Fourth:** 1D cross-section of the 2D surface model (§1.2, see §2.6), constructed from the 2D global model, three scans of which are shown (this scan = larger, darker points; adjoining scans = crosses). Differences between data and model are due primarily to residual en-route drift, which differs from scan to scan. **Fifth:** The same, but constructed from the original, uncontaminated data, demonstrating the effectiveness of this approach to RFI subtraction.

removed. This is best demonstrated by our constructed map of Jupiter, a particularly faint radio emitter (Figures 28 and 29), and Barnard’s loop (Figure 33). A similar appending procedure is available to the user for separate fields of view; however, greater care must be exercised to ensure that the data is equally calibrated, and that the edge of one map is not characterized as an outlier compared to the other map given both background-subtraction and RFI-subtraction’s underestimation near the ends of scans.

Finally, we test RFI-subtraction on a daisy mapping pattern to verify the functionality on non-rectangular mapping types (Figure 31).

## 2.6. Surface Modeling

Unlike most algorithms which use weighted averaging to regrid data onto a pixel image, our algorithm uses a weighted model to interpolate flux values between data without blurring it beyond the resolution capability of the telescope. The advantages of our model include the ability to model data after contaminant cleaning rather than having to model the data to a pixel image before contaminant cleaning can even begin. Furthermore, our algorithm allows us to model data at any time in the contaminant cleaning process as well as model the data onto a pixel density of any size. Previous algorithms often have to preselect a pixel density to streamline computa-

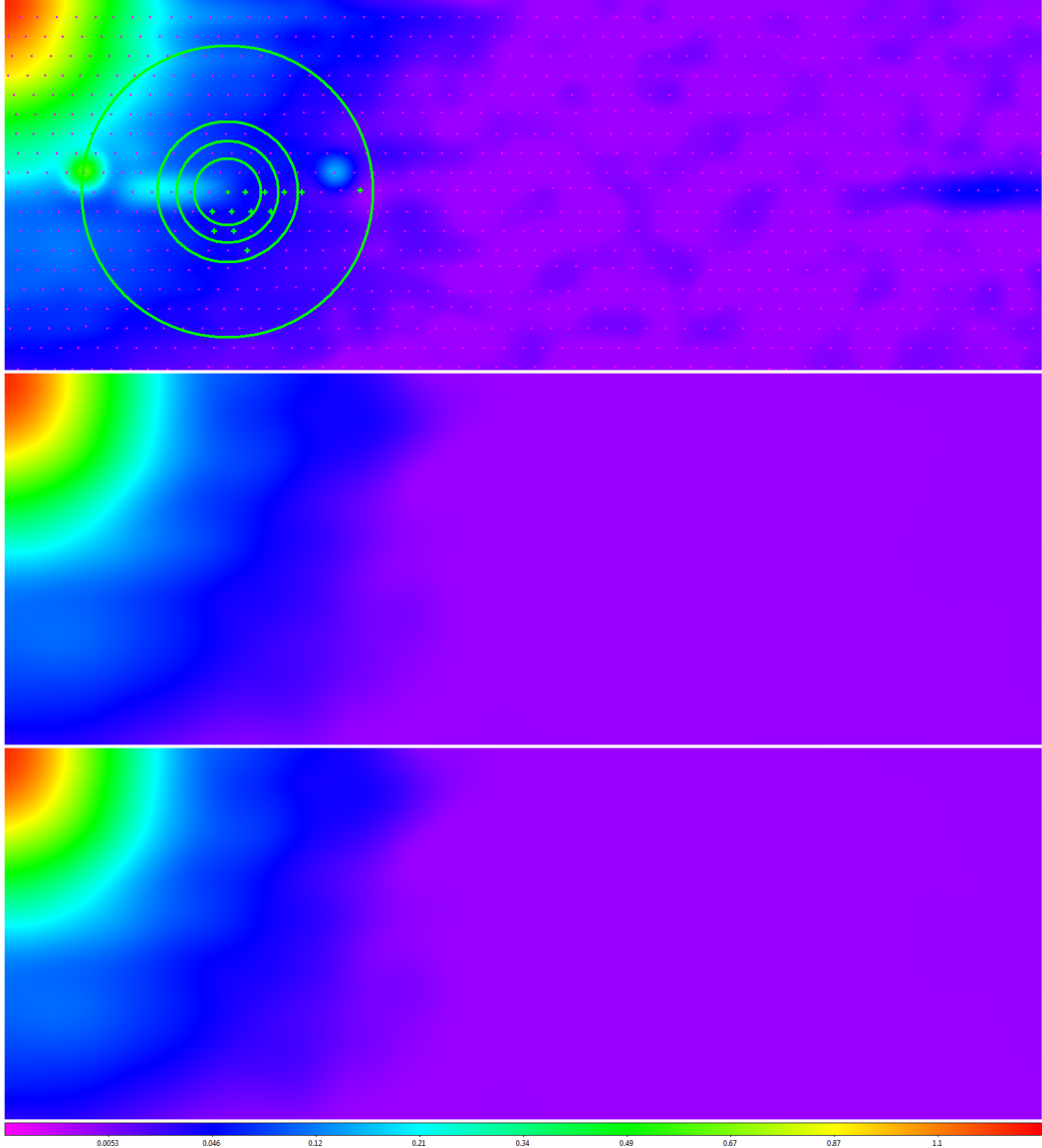


FIG. 25.— **Top:** Zoom-in of the first panel of Figure 24, but in 2D. Purple dots mark observation points. Green contours mark the 0%-25%-50%-75%- and 100%-of-peak levels of the local model. Green plusses mark observation points within the domain of the local model that were not rejected, for being too high, given the modeled noise level (§2.5.1). Locally modeled surface (§1.2, see §2.6) has been applied for visualization only. **Middle:** Zoom-in of the fourth panel of Figure 24, in 2D. **Bottom:** Zoom-in of the fifth panel of Figure 24, in 2D, which is nearly identical, despite not being contaminated with the simulated RFI.

tion time, but given that our data is already contaminant cleaned there is substantially less computation time dedicated to surface modeling than would be required by previous algorithms.

For each pixel, we fit a flexible surface model to all data that are within 1-beamwidth, weighting data that are closest to the pixel highest. We evaluate the model only at that pixel, so it only needs to fit well here. We have found using a third-order 2D polynomial is sufficient at modeling the data without blurring beyond instrument resolution while also having few enough parameters to ensure the fit is always well constrained for most sampling densities and mapping patterns:

$$z(\Delta x, \Delta y) = \sum_{i=0}^3 \sum_{j=0}^{3-i} a_{ij} (\Delta x)^i (\Delta y)^j, \quad (10)$$

where  $z$  is the locally modeled signal,  $\Delta x$  and  $\Delta y$  are angular distances from the central pixel along each coordinate, and  $a_{ij}$  are the polynomial coefficients. At this pixel, Equation 10 simplifies to  $z(0,0) = a_{00}$ , which streamlines the computation. We repeat this process for all pixels in the image.

We weight the data using a similar model to equation 9 except raised to a power:

$$w(\Delta\theta) = \begin{cases} \cos^\alpha \left( \frac{\pi \Delta\theta}{2 \text{beamwidths}} \right) & \text{if } \Delta\theta < 1 \text{ beamwidth} \\ 0 & \text{otherwise} \end{cases}, \quad (11)$$

where:

$$\alpha = -\frac{\log 2}{\log \left[ \cos \left( \frac{\pi \theta_w}{4 \text{beamwidths}} \right) \right]}, \quad (12)$$

where  $\theta_w$  is the user-defined FWHM of the weighting

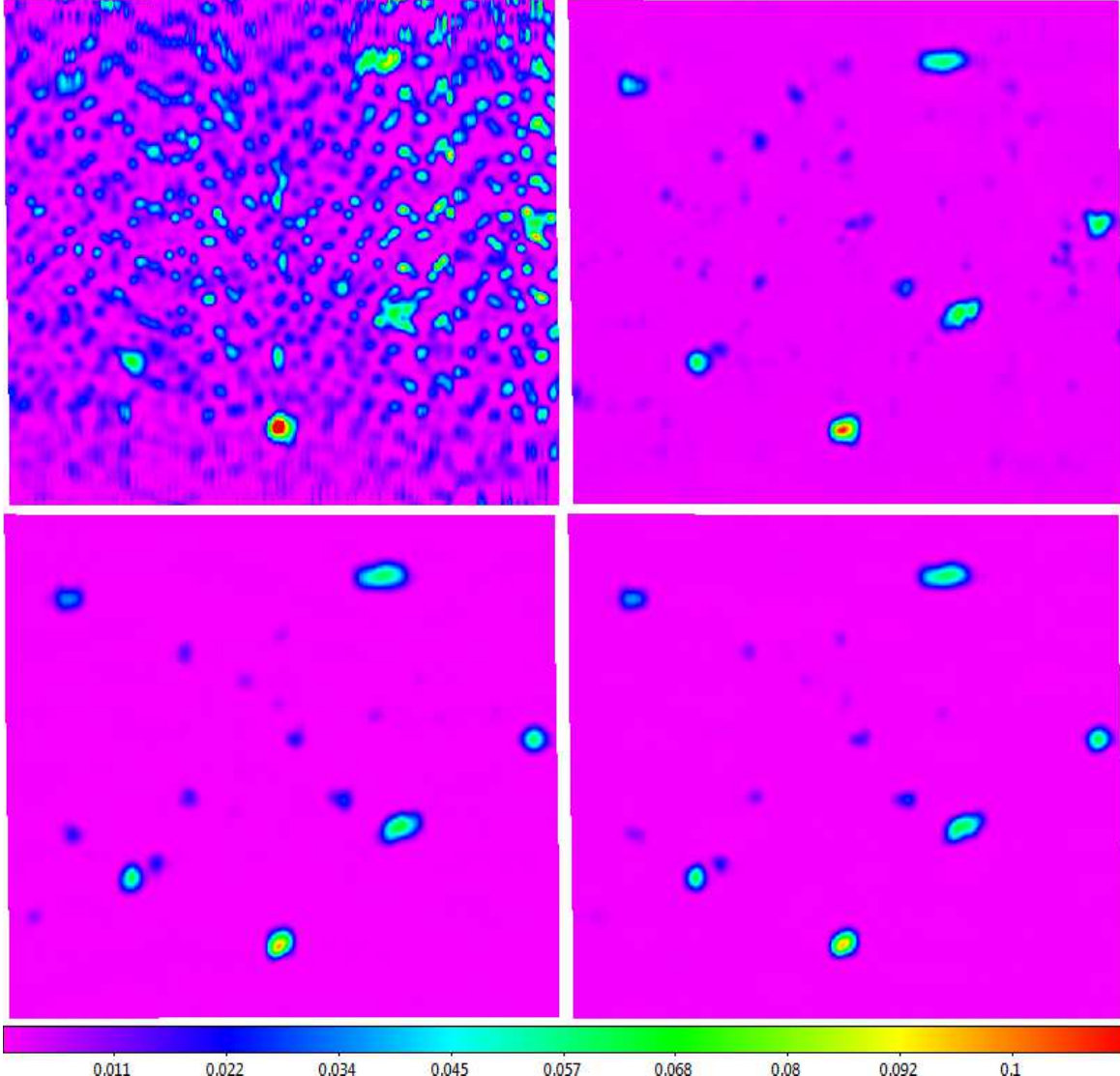


FIG. 26.— **Top Left:** Background-subtracted mapping of, from right to left, 3C 84, NRAO 1560/1650, 3C 111, 3C 123, 3C 139.1, and 3C 147, as well as fainter sources, acquired with the 40-foot in L band, using a maximum slew speed nodding pattern. The data are heavily contaminated by linearly polarized, broadband RFI, affecting only one of the receiver's two polarization channels. **Top Right:** Data from the top-left panel time-delay corrected and RFI-subtracted, with a 0.7-beamwidth scale (Table 2). **Bottom Left:** Identically processed data from the receiver's other, relatively uncontaminated polarization channel, for comparison. The RFI-subtraction algorithm is not perfect, but performs very well given the original, extreme level of contamination. **Bottom Right:** Background-subtracted and time-delay corrected data from both, equally calibrated polarization channels first appended and then jointly RFI-subtracted. Locally modeled surfaces have been applied for visualization (§1.2, see §2.6).

function. This weighting scheme allows for the weight to approach zero at the  $\theta_w = 1$  limit. This ensures no discontinuities as new data is introduced to the moving model. For smaller  $\theta_w$  values, we weight points nearest to the pixel as most significant to generate a more accurate fit. However, smaller  $\theta_w$  values also reduce the number of points to constrain the model risking the potential increase in noise and a less precisely modeled fit. We have found that Equation 10, is sufficiently flexible to reproduce most all diffraction-limited structures, to  $> 99\%$  accuracy, if  $\theta_w \leq 1/3$  beamwidths. That said, unless one is trying to visualize narrow contaminants like RFI or en-route drift, there is no advantage to surface modeling using  $\theta_w < 1/3$  beamwidths. Furthermore, for increasing values of  $\theta_w$  beyond  $1/3$ , image accuracy is reduced only marginally, while precision grows significantly more pre-

cise. For example,  $\theta_w = 1/2$ ,  $2/3$ , and  $1$  beamwidths result in only  $\approx 2\%$ ,  $\approx 4\%$ , and  $\approx 6\%$  underestimates at the source's peak, respectively, and these underestimates are almost perfectly compensated by overestimates at the source's base. Finally,  $\theta_w$  must be sufficiently large to encompass enough data to constrain equation 10. To ensure this requirement, our algorithm enforces that

$$\theta_w = \max \left\{ \theta_{min}, \min \left\{ \frac{4}{3} \times \theta_{gap}, 1 \text{ beamwidth} \right\} \right\}, \quad (13)$$

where  $\theta_{gap}$  is the largest spacing between the pixel and the nearest local points as discussed in Figure 37. For computational efficiency and modeling accuracy, we measure the value of  $\theta_{gap}$  for each data point and interpolate their values to a pixel level to be used for the afore-

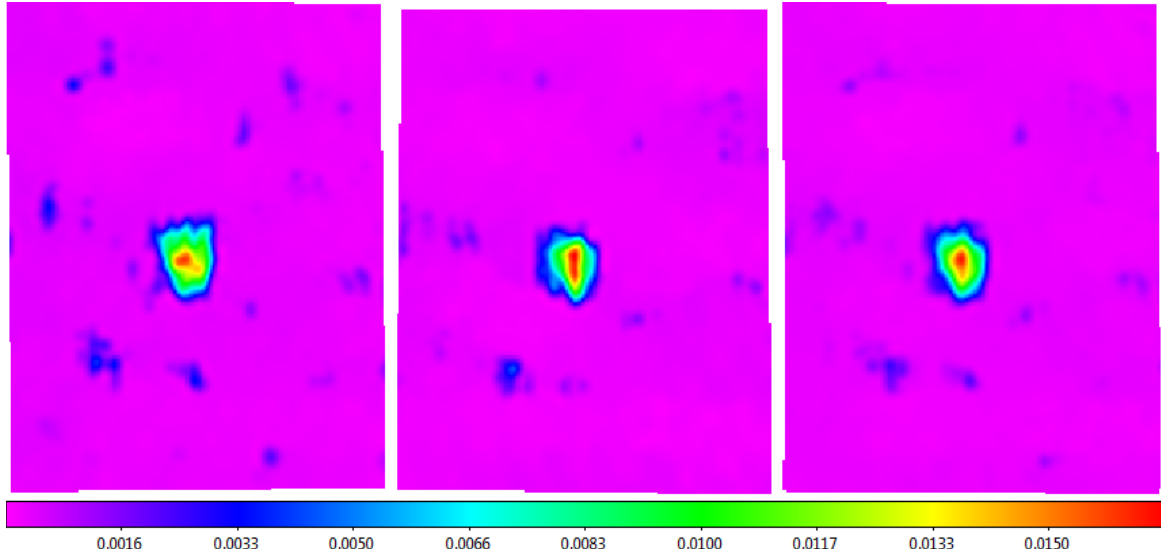


FIG. 27.— Background-subtracted and time-delay corrected 40-foot noddings of Andromeda from Figure 16 (1) separately RFI-subtracted (left and middle), and (2) appended and then jointly RFI-subtracted (right), with a 0.7-beamwidth scale (Table 2). These maps are relatively free of RFI; as such, the appended map is nearly identical to what one gets from averaging the first two maps, but is nearly twice as efficient to produce, computationally (see below). Locally modeled surfaces have been applied for visualization, with a minimum weighting scale of 1/3 beamwidths (§1.2, see §2.6).

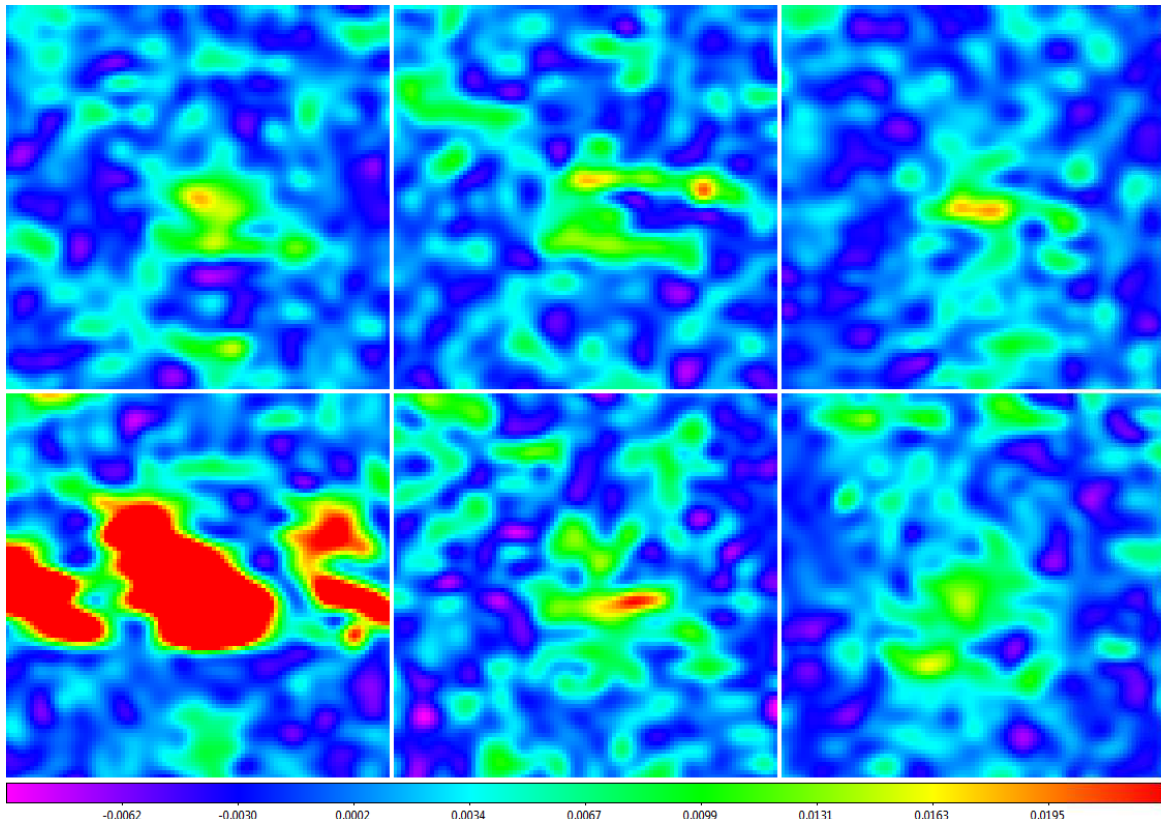


FIG. 28.— Six background-subtracted mappings of Jupiter, acquired with the 20-meter in L band, using 1/5-beamwidth rasters. Jupiter is only marginally detected in each, except for the fourth, which is significantly contaminated by RFI. Locally modeled surfaces (§1.2, see §2.6) have been applied for visualization only.

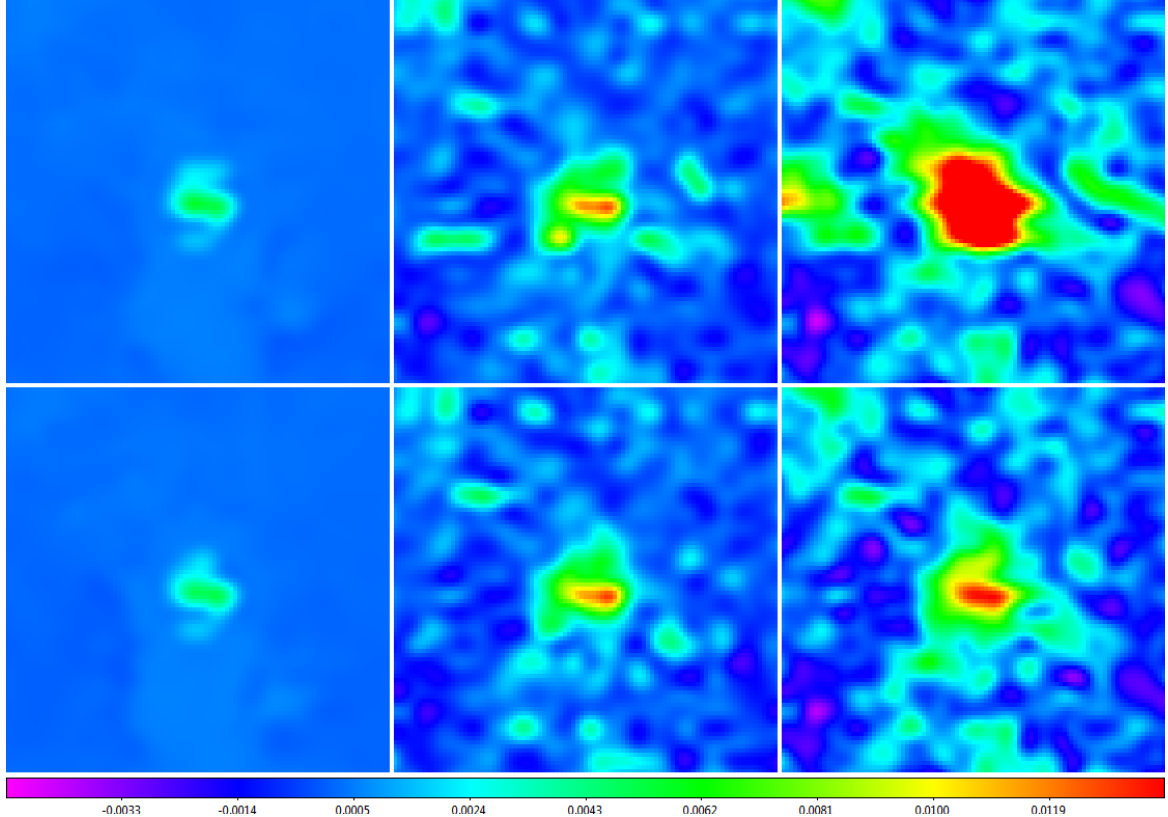


FIG. 29.— **Top Row:** The six background-subtracted mappings of Jupiter from Figure 28 appended and jointly RFI-subtracted, with 0.9- (left), 0.1- (middle), and  $\approx 0$ - (right) beamwidth RFI-subtraction scales. **Bottom Row:** The same, but excluding the fourth, significantly RFI-contaminated mapping from Figure 28. Smaller RFI-subtraction scales recover more near noise-level signal. Because multiple 0.2-beamwidth mappings are used, the RFI-subtraction scale can be as low as 0.1-beamwidths and still be completely effective at eliminating RFI. Locally modeled surfaces have been applied for visualization, with a minimum weighting scale of 1/3 beamwidths (§1.2, see §2.6).

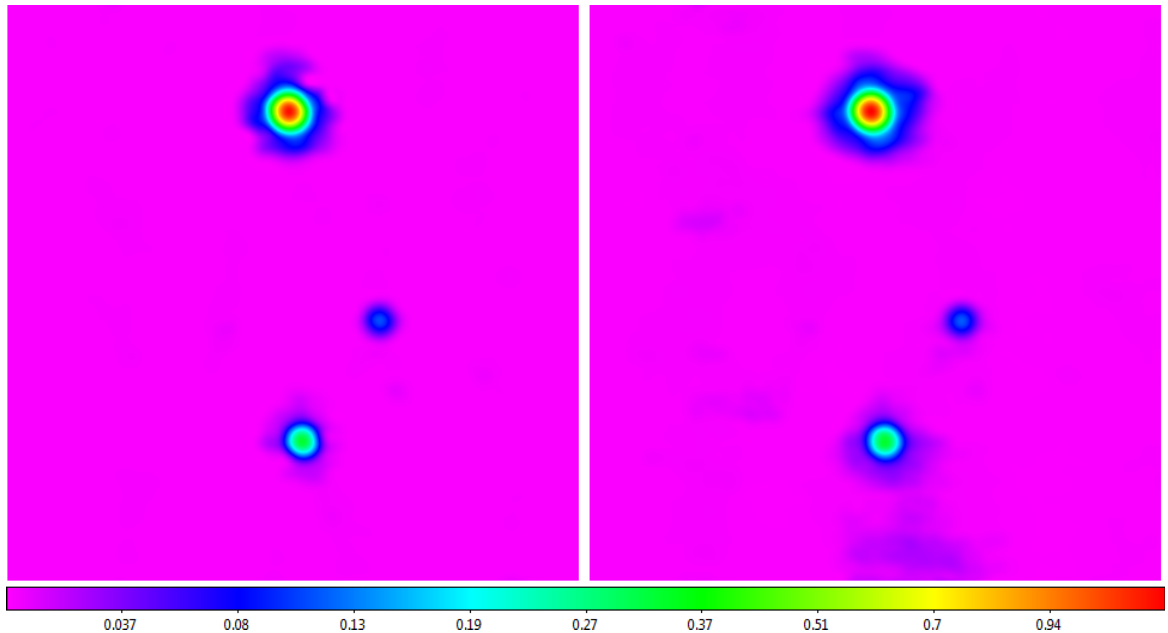


FIG. 30.— 20-meter L-band raster from Figure 5 background-subtracted, with 7- (left; Table 1) and 24- (right) beamwidth scales (Figure 15), and RFI-subtracted, with a 0.9-beamwidth scale (Table 2). RFI, both long-duration intersecting 3C 273 and short-duration near Virgo A, as well as en-route drift across the entire image, are successfully eliminated. Locally modeled surfaces have been applied for visualization, with a minimum weighting scale of 2/3 beamwidths (§1.2, see §2.6). Hyperbolic-arcsine scaling is used to emphasize fainter structures.

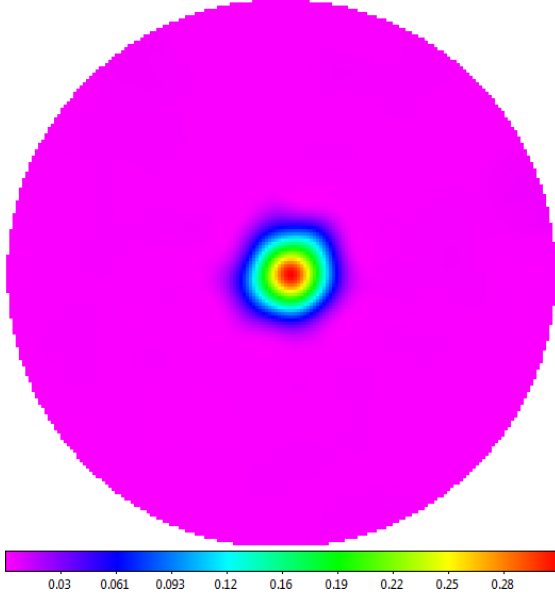


FIG. 31.— Background-subtracted 20-meter X-band daisy of 3C 84 from Figure 17 RFI-subtracted, with a 0.8-beamwidth scale (Table 2). Locally modeled surfaces have been applied for visualization, with a minimum weighting scale of 2/3 beamwidths (§1.2, see §2.6).

mentioned surface modeling procedure. If it is determined there is insufficient data to constrain the model within the  $\theta_w$  radius, we excise the pixel from the data set. This procedure is generalized to all mapping patterns and coordinate types as demonstrated by its success of a daisy mapping (Figure 31) and in converting from equatorial to galactic coordinates (Figure 36).

### 2.7. Default Data Products

Upon completion of each 20-meter mapping, Skynet produces six default data products:

1. **Raw Maps** use the pre-processed data and a  $\theta_w = 0$  and only apply the surface modeling routine to the data to visualize sub-beamwidth contaminants.
2. **Contaminant-Cleaned Maps** surface model using  $\theta_{min} = 2/3$  after the data has undergone background subtraction, time-delay correction, and RFI-subtraction.
3. **Path Maps** plot one point on the center of each coordinate to show the mapping pattern. We generate two path maps, one prior to time-delay correction, and one after the correction—both include points that were excised through RFI-subtraction.
4. **Scale Maps** are the calculated weighting scale used for surface modeling at each pixel.
5. **Weight Maps** record the weighted number of data points that went into the model fit. This includes the product of the proximity-dependent weight and the number of dumps that contributed to each of the included points, divided by a number that corrects for the non-independence of the value over a scale that is related to the RFI-subtraction scale.

6. **Correlation Maps** record the scale over which pixel data are correlated, a useful metric for photometric error bars.

The path map, scale map, weight map, and correlation map of Figures 17 and 31 are showcased in Figure 38.

### 3. APERTURE PHOTOMETRY

In this section, we present an aperture photometry algorithm which we use to test the accuracy of our small-scale structure maps. Similar to optical frequencies, photometry can be performed using an annulus and aperture to extract a photometric value. To begin, we first centroid the aperture on the source of interest by fitting a second-order version of equation 10, with a fixed weighting scale of  $\theta_w = 1/3$  beamwidth, to every pixel within a 1-beamwidth radius of the first-guess pixel. The centroid is given by the extremum of this function. This procedure is iterated until convergence.

Once the centroid is identified, we then measure the background noise  $\mu$ , the standard deviation of the background level  $\sigma$ , and the uncertainty in our measurement of the background level,  $\mu_\sigma$ . These metrics are calculated using the weight map and contaminant-cleaned map as well as RCR to eliminate pixels contaminated by Airy rings, other sources, etc. We then sum the pixel values in the aperture, subtracting the weighted-mean background level from each pixel.

The total photometric error bar is then given by:

$$\sigma_{phot} = f_{\sigma_{phot}} \sqrt{\sigma^2 \sum_{i=1}^{N_{ap}} \frac{\langle w \rangle_{an}}{w_i/N_i} + (N_{ap}\sigma_\mu)^2}, \quad (14)$$

where the sum is over the number of pixels in the aperture,  $N_{ap}$ ,  $w_i$  is each pixel's weight-map value,  $\langle w \rangle_{an}$  is the average weight-map value of the pixels in the annulus that were used to measure  $\sigma$ ,  $N_i$  is a number that, at least approximately, corrects for the non-independence of the  $i$ th-pixel's value over both the RFI-subtraction and surface-modeling (weighting) scales, and  $f_{\sigma_{phot}}$  is an empirically determined correction factor.

We now proceed to test the accuracy of our photometry algorithm on the simulated sources. Using recommended processing parameters, we find that the measured values underestimate the true values marginally for the highest-S/N sources, but increasingly so for lower-S/N sources. These underestimates are significant relative to the expected level of uncertainty—provided by the 100 re-simulations of the data in which the noise and en-route drift had been randomized. This is to be expected, however, as the RFI-subtraction routine systematically dims the source particularly if the RFI-subtraction scale is high. A similar effect occurs when  $\theta_w$  is large. Having measured these effects for a large range of RFI-subtraction scale values and values of  $\theta_w$  we have assembled the following empirical correction factor:

$$f_{phot} = \exp \left[ 0.22 \left( \frac{\theta_{ap}}{2.5} \right)^{0.52} \left( \frac{z_{peak}}{1000\sigma} \right)^{-1.20} \left( \frac{\theta_{ap}}{2.5} \right)^{-0.39} \times \Theta(\theta_{RFI}, \theta_{min}, \theta_{ap}) \right], \quad (15)$$

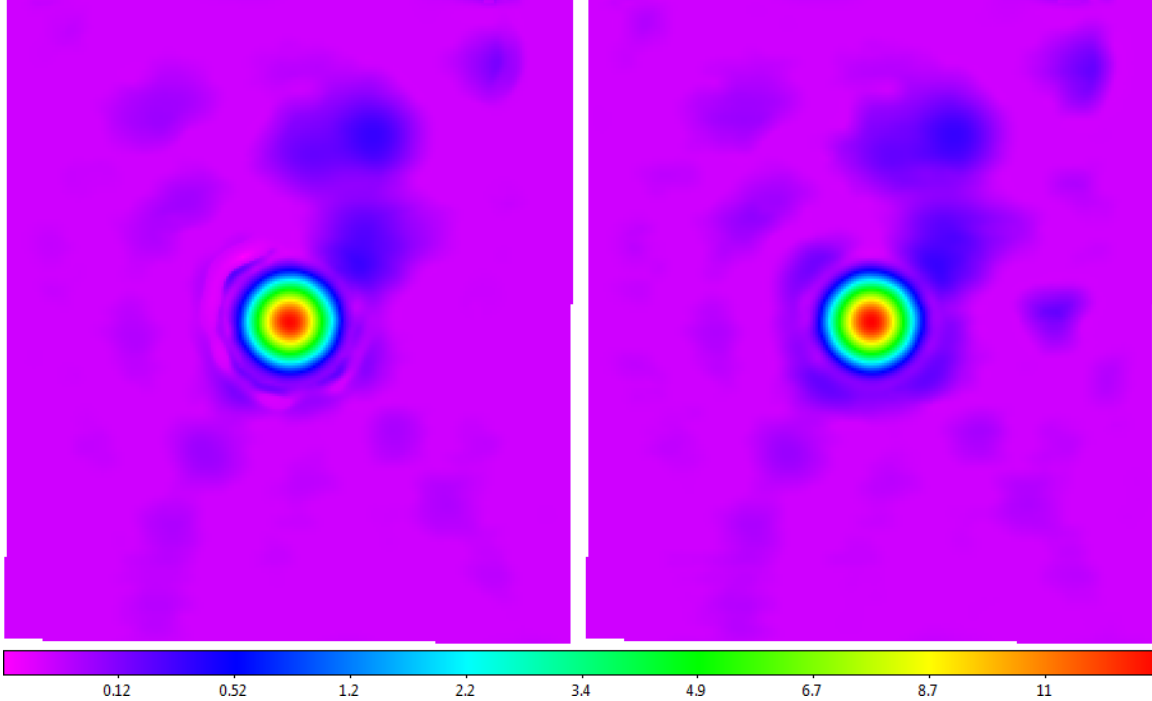


FIG. 32.— Background-subtracted 20-meter L-band raster of Cassiopeia A from Figure 35 RFI-subtracted, (1) with the maximum recommended RFI-subtraction scale from Table 2 (0.8 beamwidths), which partially eliminates the first Airy ring (left), and (2) with half of this scale, which retains this structure (right). Locally modeled surfaces have been applied for visualization, with a minimum weighting scale of 1/3 beamwidths (§1.2, see §2.6). Square-root scaling is used to emphasize fainter structures.

TABLE 3  
APERTURE PHOTOMETRY OF SIMULATED SOURCES FROM §3.3 AND §3.6<sup>a</sup>

Source Ratio	Brightness			Percent Error		Error Bars (%)			Total (from calculation and correction)
	Measured	Corrected	True	Measured	After Correction	Internal Calculated	External Simulated (from correction)		
2 / 1	0.252	0.252	0.255	-1.3	-1.0	0.2	0.1	0.2	0.2
3 / 1	0.110	0.111	0.112	-1.7	-0.2	0.2	0.4	0.6	0.7
4 / 1	0.061	0.064	0.062	-2.5	2.7	0.4	0.8	2.0	2.0
5 / 1	0.038	0.040	0.040	-5.2	-0.1	1.0	1.0	2.0	2.2
6 / 1	0.028	0.032	0.031	-12.4	1.6	1.7	0.7	5.3	5.6
7 / 1	0.018	0.026	0.022	-18.8	16.4	1.9	3.3	10.6	10.8
8 / 1	0.016	0.019	0.020	-23.1	-4.6	2.1	1.3	7.3	7.6
9 / 1	0.009	0.015	0.012	-26.8	22.1	2.7	2.3	13.1	13.4
10 / 1	0.007	0.012	0.010	-35.1	14.8	2.3	2.5	13.8	14.0

<sup>a</sup> Relative to the brightest source. This particular data set was generated using the less-winged beam function of Equation 9 and Figure 23, and included the exact same contaminants that we use in Figure A.7. The data were then processed using a 6-beamwidth background-subtraction scale, a 0.5-beamwidth RFI-subtraction scale, a 0.5-beamwidth surface-modeling (minimum weighting) scale, and the noise-level prior. Aperture photometry was carried out using a 2-beamwidth diameter aperture and an annulus of 2- and 10-beamwidth inner and outer diameters, respectively. (We have repeated these measurements for more-winged beam functions, for a wide range of background-subtraction, RFI-subtraction, and minimum-weighting scales, both with and without the noise-level prior, and for a wide range of aperture and annulus diameters, with similar results.) Measurements are presented both before and after correcting for dimming caused by the RFI-subtraction algorithm, and to a lesser extent, by the surface-modeling algorithm (see Equation 20 below), which affects the lower-S/N sources in particular. We calculate internal error bars using Equation 17 above, and these are consistent with those measured by re-simulating, re-processing, and re-photometering this data set 100 times, where we have randomized the noise and en-route drift in each simulation. We calculate external error bars as part of the low-S/N dimming correction (see Equation 22 below). Total error bars are given by adding our internal and external error bars in quadrature, and these are consistent with the measurement errors in our post-correction photometry (except for the highest-S/N source, which suggests that our uncertainty is probably never less than ~1%, regardless of Equations 17 and 20). Note, in this example, the internal error bars are small – often negligibly small – compared to the external error bars. However, this is because these (simulated) sources are very densely sampled by this mapping; with lower-density mappings, the internal error bars can be much larger. Also note that when measuring a source’s signal-to-noise, only its internal error bar matters; the rest is calibration uncertainty.

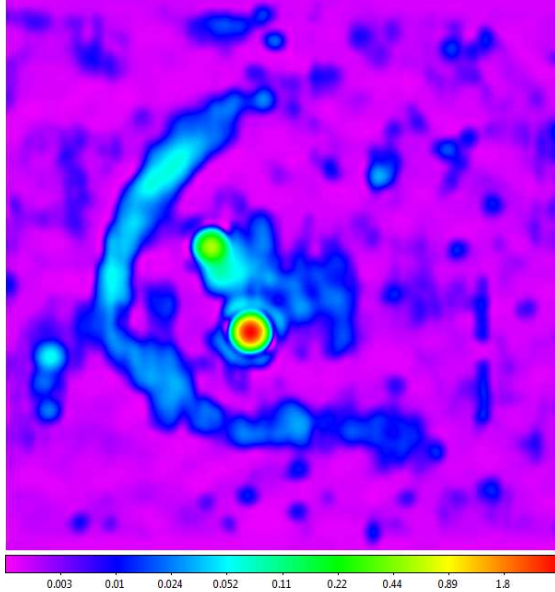


FIG. 33.— Four 20-meter L-band rasters of Orion A, Orion B, and Barnard’s Loop, separately background-subtracted, with a 20-beamwidth scale (larger than the minimum recommended scale from Table 1, given the size of Barnard’s Loop), time-delay corrected, appended, jointly RFI-subtracted, with a 0.4-beamwidth scale (to preserve Airy rings), and surface-modeled, with a minimum weighting scale of 2/3 beamwidths. Logarithmic scaling is used to emphasize Barnard’s Loop and fainter sources.

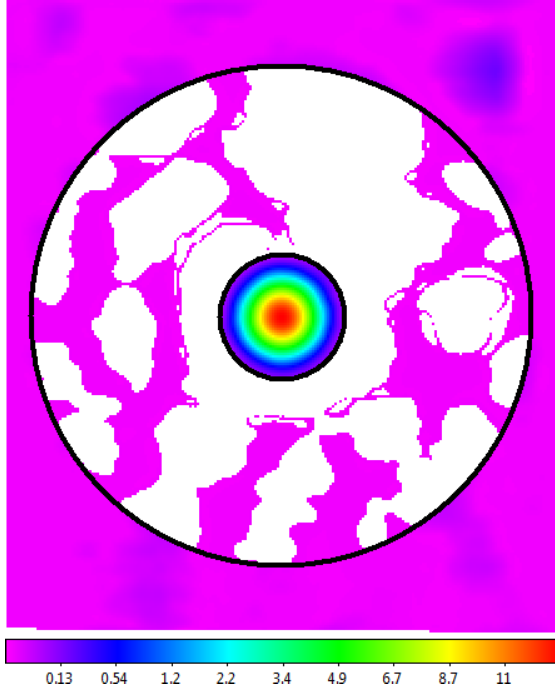


FIG. 34.— 2.5-beamwidth diameter aperture and 10-beamwidth diameter annulus that we use in Table 4, centroided on Cassiopeia A, from the right panel of Figure 32. Outlying pixels within the annulus, corresponding to Airy rings, other sources, etc., have been eliminated (compare to Figure 32). Square-root scaling is used to emphasize fainter structures.

where  $z_{peak}$  is the signal level at the peak of the source,<sup>7</sup>  $\sigma$  is the standard deviation of the pixel values in the annulus from above,  $\theta_{RFI}$  and  $\theta_{min}$  are measured in beamwidths,  $\theta_{ap} = \min\{\text{aperture diameter in beamwidths}, 2.5\}$ , and:

$$\Theta(\theta_{RFI}, \theta_{min}, \theta_{ap}) = \theta_{RFI}^{2.64\left(\frac{\theta_{ap}}{2.5}\right)^{-0.54}} + 0.34 \left(\frac{\theta_{ap}}{2.5}\right)^{0.73} \theta_{min}^{1.66\left(\frac{\theta_{ap}}{2.5}\right)^{-0.18}}. \quad (18)$$

The uncertainty in  $f_{phot}$  is approximately given by:

$$\sigma_{f_{phot}} = 0.082 \left(\frac{\theta_{ap}}{2.5}\right)^{0.32} \left(\frac{z_{peak}}{1000\sigma}\right)^{-1.35\left(\frac{\theta_{ap}}{2.5}\right)^{-0.08}} \times \Theta(\theta_{RFI}, \theta_{min}, \theta_{ap}). \quad (19)$$

We find that these expressions hold relatively independently of whether the beam function is narrow- or broad-winged. When applied to the measured values, we find that the values fall within one total error bar of their true values (Table 3).

Finally, we proceed to test the accuracy of our small-scale structure mapping algorithm by photometering real sources, particularly the calibration sources Cassiopeia A, Cygnus A, Taurus A, and Virgo A, and compare them to previously modeled expectations. We took 24 observations of each source over a few days, photometered each with a 2.5-beamwidth diameter aperture, and took the ratios of these values, and then averaged these ratios as done previously in Trotter et al. (2017). We list these values in Table 4 and they match their expected values within uncertainties.

#### 4. CONCLUSION

In summary, we have presented an algorithm that proceeds in the following manner:

1. Our algorithm models background contamination locally using quadratic regression while also making use of a new outlier rejection algorithm, robust Chauvenet outlier rejection, to remove significant fractions of signal from en-route drift, long-duration RFI, and elevation-dependent signal.

<sup>7</sup> This is given by summing the  $\mu$ -subtracted pixel values in the aperture out to a user-selected radius, and dividing this by the sum of the peak-normalized beam function, evaluated at these same locations. For the cosine-squared beam function in Figure 23, the latter sum is approximately given by:

$$\frac{1}{\theta_{pix}^2} \left( \frac{\pi\theta^2}{2} + \frac{\cos \pi\theta}{\pi} + \theta \sin \pi\theta - \frac{1}{\pi} \right), \quad (16)$$

where  $\theta < 1$  is the user-selected radius in beamwidths, and  $\theta_{pix}$  is the number of beamwidths per pixel (our default value is 0.05; §2.6). For the Gaussian beam function in Figure 23, this is instead given by:

$$\frac{1.13309 - 1.13309e^{-2.77259\theta^2}}{\theta_{pix}^2}. \quad (17)$$

These two expressions are nearly identical for  $\theta < 0.7$  beamwidths, and differ by only  $\approx 13\%$  at  $\theta = 1$  beamwidth. If the point-spread function is not known, we recommend using either of these functions, but with  $\theta = \min\{0.7, \theta_{ap}/2\}$ .

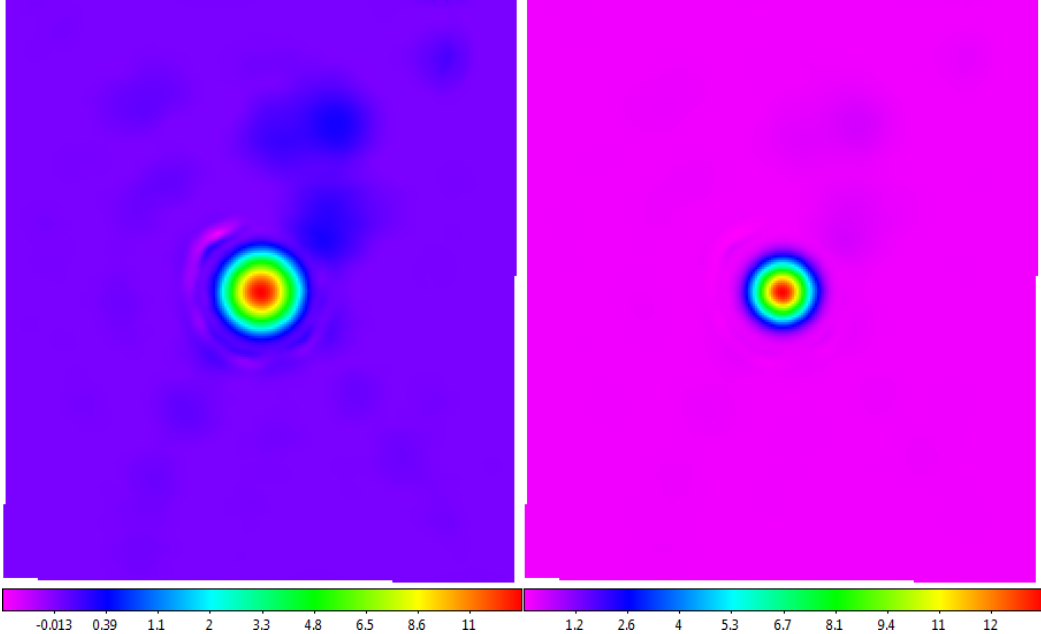


FIG. 35.— The left panel of Figure 32, instead processed without the noise-level prior (see Footnote 27), and visualized with square-root scaling on the left, and with regular, linear scaling on the right. The surface model undershoots at the base of this high-S/N, well-focused, point source, especially where the first Airy ring has been partially eliminated by the RFI-subtraction algorithm. Consequently, the noise-level prior is normally included (Figure 32). Note, however, that even without the noise-level prior, this is a small effect, and is only barely noticeable when visualized on regular, linear scaling (right).

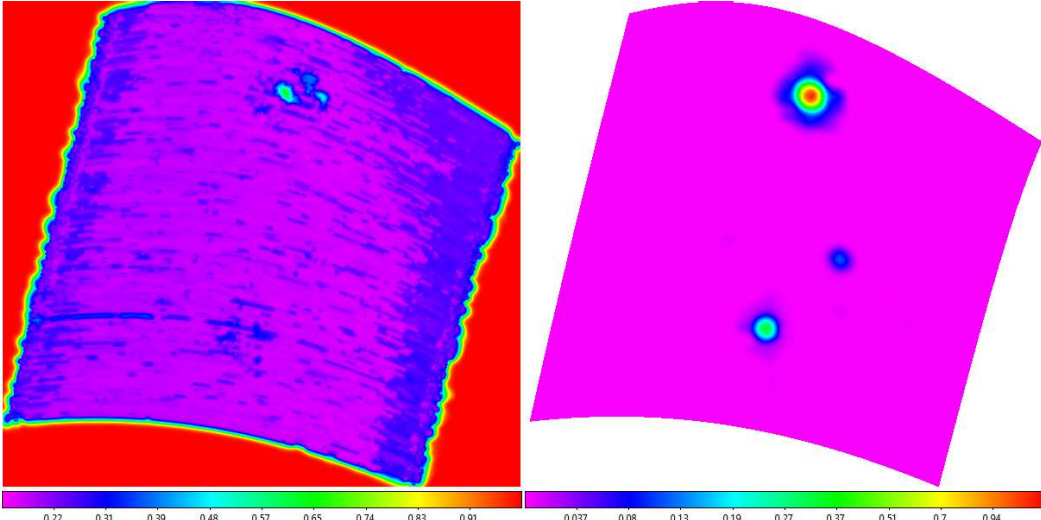


FIG. 36.— **Left:** The weighting scale map from the top-right panel of Figure 37, but instead processed after converting to Galactic coordinates. **Right:** The corresponding final image, also processed in Galactic coordinates, after imposing a minimum weighting scale of 2/3 beamwidths, so it can be compared to the left panel of Figure 30. In Figure 30, we process the same data, but in its original, equatorial coordinate system. Furthermore, this field is at high Galactic latitude, and consequently serves as a good example of the equal-areas and equal-distances properties of our sinusoidal projection (see below). Equal areas means that sources cover the same number of pixels, and consequently should yield approximately the same photometry (see §3): The three sources in this map yields the same photometry as in the left panel of Figure 30 to within 3%, despite the greater (diagonal) distortion that these sources can experience at high Galactic latitudes. Equal distances refers to distances along horizontal lines, as well as along the central vertical axis, being distortion-free.

2. Once the underlying background biases have been removed, our algorithm offers a solution to the time-delay constant imposed by both the 20-meter and 40-foot telescope through performing a cross-correlation in fourier space to determine the appropriate correction factor.
3. After the data background bias is eliminated and its correlation aligned, our algorithm generates two-dimensional cosine models to investigate sub-

beamwidth contaminant structure.

4. Based on the constructed models from RFI-subtraction, our algorithm proceeds to use weighted modeling as an alternative to weighted averaging to interpolate data onto a pixel grid. This procedure models data accurately without blurring sources beyond the resolution capabilities of the telescope.

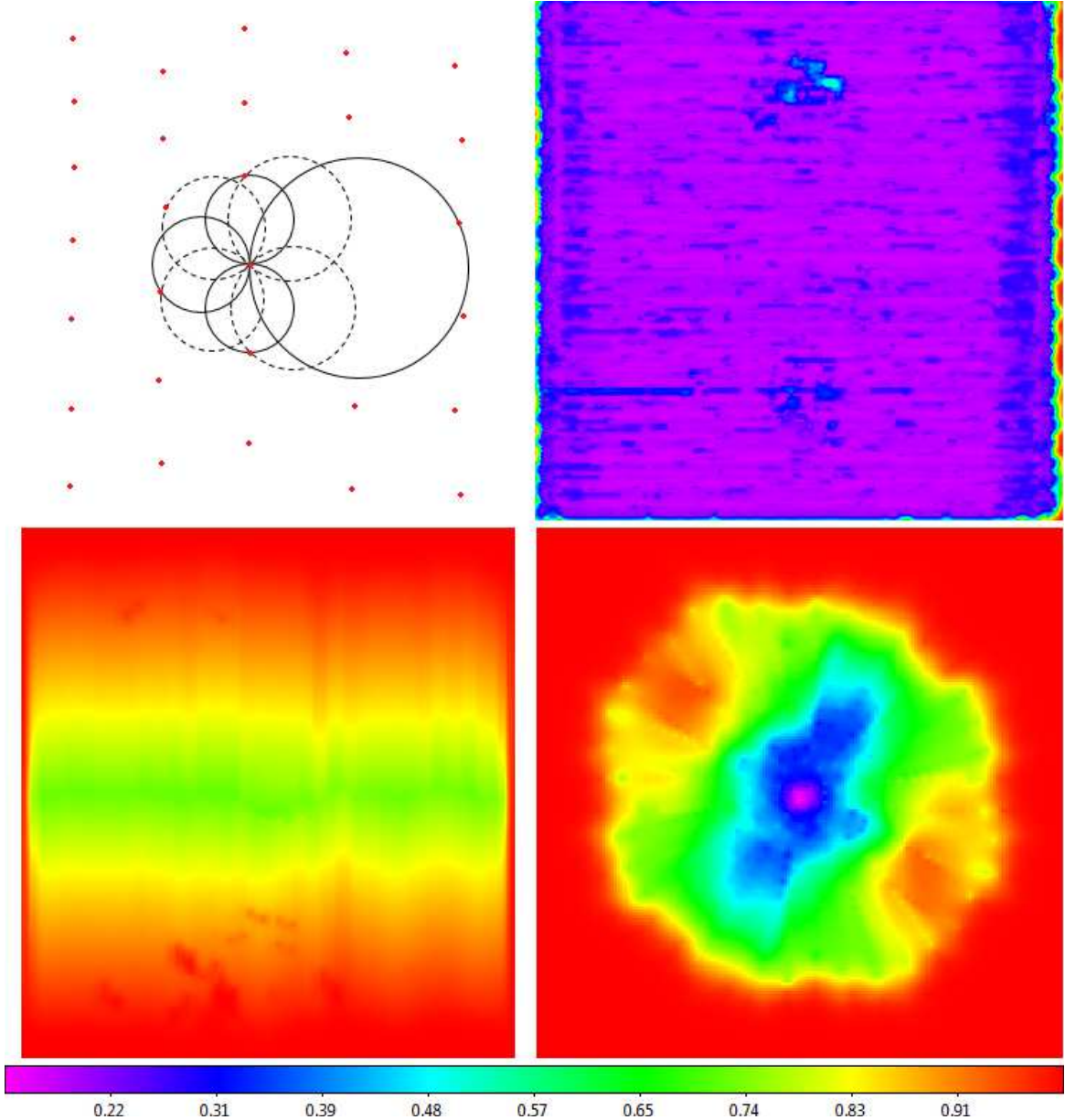


FIG. 37.— **Top Left:** From each data point, we “blow a bubble” in each of the coordinate system’s eight cardinal directions, until it intersects another data point that is within  $45^\circ$  of the blow direction, and that is more than a minimum angular distance away. We determine this minimum angular distance by taking all angular distances between consecutive measurements in the observation and performing outlier rejection on them, determining the minimum angular distance that is not rejected.<sup>a,b,c</sup> Employing this minimum angular distance decreases computation time, and prevents undersized bubbles from being blown, due to data-point clustering, usually at the ends/beginnings of scans, where the telescope changes direction. We take the largest bubble’s diameter as our local measure of  $\theta_{gap}$ , from it calculate  $\theta_w$  (Equation 14), and then interpolate between these values at each pixel in the final image (Footnote 28). **Top Right:** Raster example: Resulting values of  $\theta_w = \min\{\frac{4}{3} \times \theta_{gap}, 1\}$  for the 20-meter horizontal raster from Figures 5, 23, and 38. Larger gaps are measured where the telescope’s momentum caused it to overshoot when changing directions, near the ends/beginnings of scans, and where the wind pushed the telescope across its direction of motion. Larger gaps are also measured where the RFI-subtraction algorithm removed data points, both due to RFI (e.g., the scan intersecting 3C 273), and in the outskirts of the beam pattern around Virgo A. **Bottom Left:** Nodding example: Resulting values of  $\theta_w = \min\{\frac{4}{3} \times \theta_{gap}, 1\}$  for the 40-foot nodding from Figure 18. This is a sparse mapping, with only  $\approx 0.4$ -beamwidth gaps between scans at its middle declination, which, since this is a nodding pattern, yields gaps that are twice as large at the top and bottom of the mapping (Figure 2, middle panel). **Bottom Right:** Daisy example: Resulting values of  $\theta_w = \min\{\frac{4}{3} \times \theta_{gap}, 1\}$  for the 20-meter daisy from Figures 25 and 44. The pattern is asymmetric, because gravity’s pull on the telescope resulted in narrower petals along the lower-left to upper-right diagonal, and wider petals orthogonally (see Figure 2).

<sup>a</sup>For daisies, the telescope’s slew speed is variable, with the smallest angular distances between consecutive measurements occurring at the ends/beginnings of scans, which is also where this is most difficult to measure accurately: The telescope’s rapid transition between deceleration and acceleration at the ends/beginnings of scans is often messy, resulting in data-point clustering. Consequently, we instead measure these angular distances at the center of each scan, where the telescope is moving fastest, with minimum acceleration/deceleration, and then divide by half of the number of scans, which gives what these angular distances should have been at the ends/beginnings of scans.

<sup>b</sup>We reject outliers as described in §8 – §10 of Maples et al. 2017, using iterative bulk rejection followed by iterative individual rejection (using the mode + broken-line deviation technique, followed by the median + 68.3%-value deviation technique, followed by the mean + standard deviation technique), using the smaller of the low and high one-sided deviation measurements. Data are weighted equally.

<sup>c</sup>In the case of appended mappings (§2.5), we adopt the minimum of each mapping’s minimum non-rejected angular distance, in each overlap region.

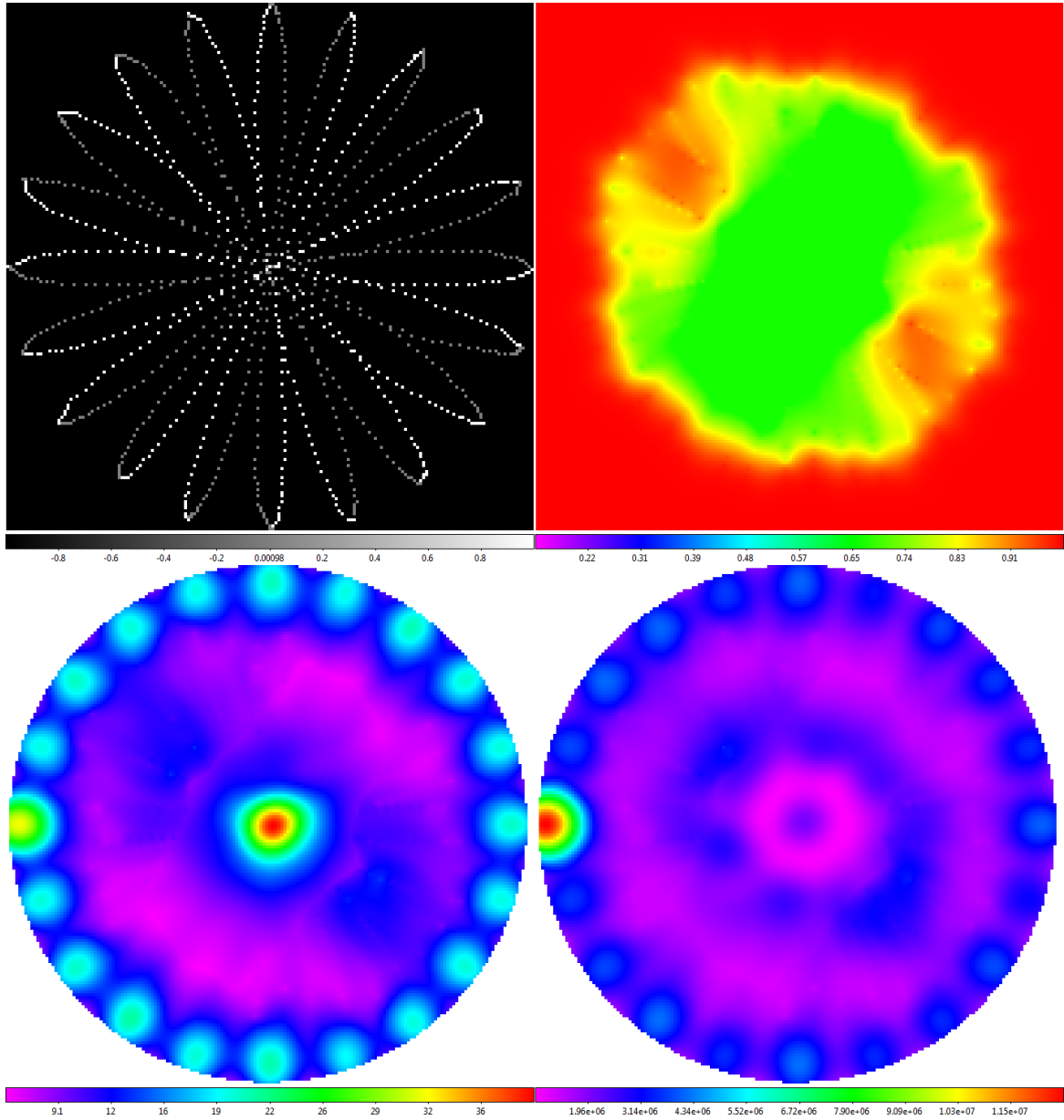


FIG. 38.— **Top Left:** Path map of the 20-meter X-band daisy from Figures 17 and 31. This is a 20-petal daisy, though the user may select as few as four petals (however, see §3). The path began and ended on the left edge, and some points, particularly near the center, have been removed by the RFI-subtraction algorithm. Alternating scans alternate between white and gray. **Top Right:** The corresponding scale map for our default minimum weighting scale of  $\theta_{min} = 2/3$  beamwidths (Equation 13), which can be compared to the top-right panel of Figure 37, where  $\theta_{min} = 0$  beamwidths. This is the scale map that was used to surface-model Figure 31. The exterior yellow, orange, and red regions, corresponding to  $\theta_w > 3/4$  beamwidths, are not appropriate for photometry, but this is not a problem because the source does not extend this far out (Figure 31). **Bottom Left:** Weighted number of data points that contributed to each pixel when surface-modeling Figure 31, given the path map and the scale map. Extra data were acquired at the telescope's start/stop position, on the left edge. **Bottom Right:** The full weight map, which includes weights for each of the post-RFI subtraction values that were fitted to when surface-modeling Figure 31. Less information informs these values in the vicinity of the source. Weight maps are important (1) when stacking images, since not all regions are equally well determined, and (2) when doing photometry, both when determining the background level and when calculating error bars.

TABLE 4  
FLUX-DENSITY RATIOS OF PRIMARY CALIBRATION SOURCES<sup>a</sup>

Source Ratio	Measured Flux-Density Ratio (Average of 24)	Modeled Flux-Density Ratio (Baars et al. 1977)	Modeled Flux-Density Ratio (Trotter et al. 2017)
Cas A / Cyg A	$1.1046 \pm 0.0071$	$0.951 \pm 0.091^b$	$1.104 \pm 0.018$
Tau A / Cyg A	$0.5348 \pm 0.0043$	$0.592 \pm 0.065^b$	$0.5287 \pm 0.0078$
Vir A / Cyg A	$0.1411 \pm 0.0071$	$0.135 \pm 0.016$	$0.1370 \pm 0.0021$

<sup>a</sup> Measured from 96 (24 for each source) 20-meter L-band maps, each processed separately with recommended/default settings, and expected values from temporal and spectral models that have been fitted to nearly 60 years of measurements. For each measurement of Cas A, Tau A, and Vir A, we took the measurement of Cyg A that was closest in time, usually within hours, and vice versa, to minimize differences in calibration, took their ratio, and averaged these ratios, rejecting outliers using Maples et al. (2017), as described in Trotter et al. (2017). Our averaged ratios agree with the expected ratios to within the uncertainties.

<sup>b</sup> Baars et al. (1977) overestimated the fading of Cas A, and did not model (and hence underestimated) the fading of Tau A. These have been corrected, and the spectral models of Baars et al. (1977) also improved upon, in Trotter et al. (2017; see also Reichart & Stephens 2000).

- Finally, our algorithm provides a means to perform basic photometric analysis on radio images that successfully model major calibration sources within anticipated error bars.

I gratefully acknowledge my adviser Daniel Reichart in his continued support throughout these research pursuits. In addition, I would like to acknowledge the North Carolina Space Grant Consortium, UNC-Chapel Hill's Office for Undergraduate Research, and NSF grants and awards: ESP 0943305, MRI-R<sup>2</sup> 0959447, AAG 1009052, 1211782, and 1517030, ISE 1223235, HBCU-UP 1238809, TUES 1245383, and STEM+C 1640131 for helping fund this project. Furthermore, I would like to acknowledge all former students who have contributed to the success of this project, particularly Dylan Dutton, Michael Maples, and Travis Berger who were actively involved in the early development and testing of many of the aforementioned techniques.

APPENDIX  
A. BACKGROUND SUBTRACTION VERIFICATION

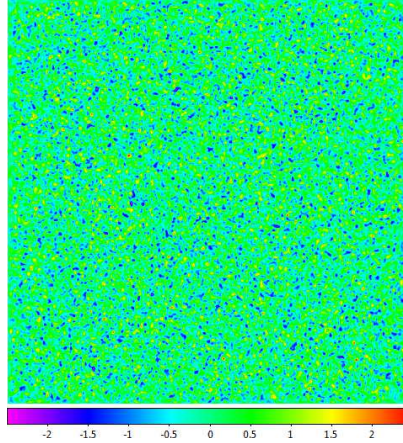


FIG. A.1.— 20-meter 1/10-beamwidth horizontal raster approximately 24-beamwidths in size replaced with Gaussian random noise with mean of zero and standard deviation of one. Locally modeled surface (§1.2, see §2.6) has been applied for visualization only.

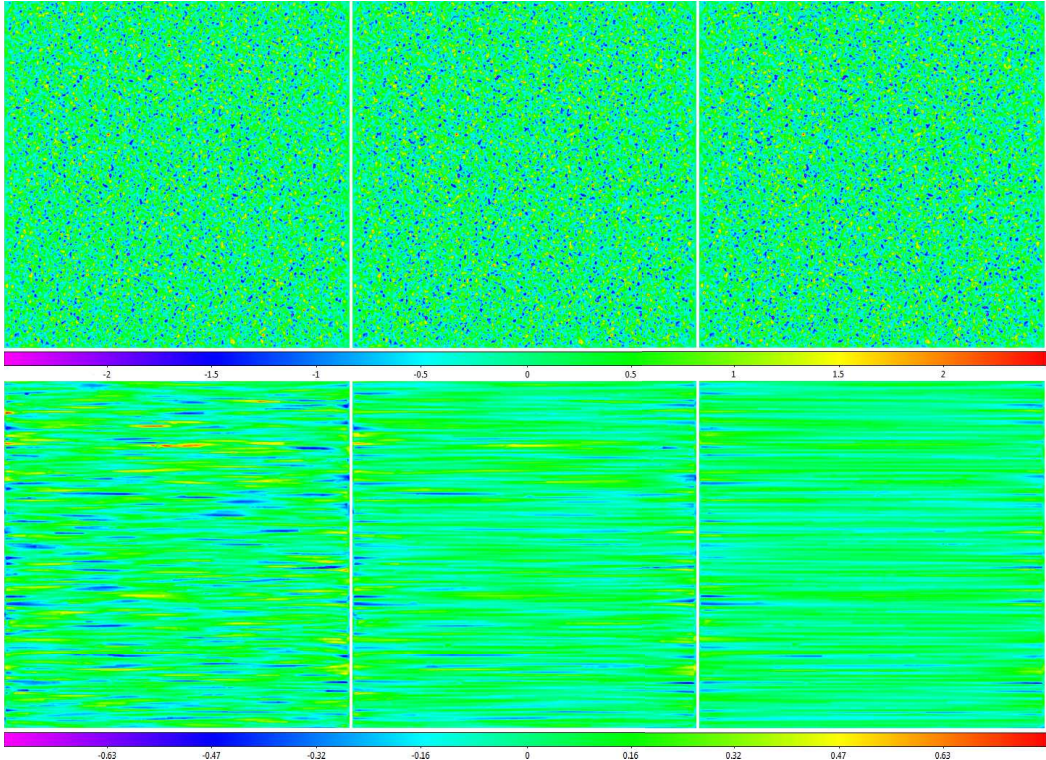


FIG. A.2.— **Top Row:** Data from Figure A.1 background-subtracted, with 6- (left), 12- (middle), and 24- (right) beamwidth scales. **Bottom Row:** Data from the top row minus the data from Figure A.1 (residuals). Background-subtracted data are not biased high nor low. To first order, the noise level of the background-subtracted data is  $\approx 98.0\%$  (left),  $\approx 98.8\%$  (middle), and  $\approx 99.3\%$  (right) of that of the original data, and the RMS of the residuals is only  $\approx 20.1\%$  (left),  $\approx 15.4\%$  (middle), and  $\approx 12.3\%$  (right) of the noise level of the original data (see Figure 13 for second-order effect). Locally modeled surfaces (§1.2, see §2.6) have been applied for visualization only.

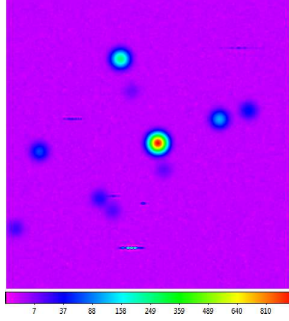


FIG. A.3.— Simulated data from Figure A.1 with added point sources and short-duration RFI. The point sources are simulated using a Gaussian beam pattern, and the short-duration RFI is produced using the absolute value of superposition of varying sine functions multiplied by a short-duration Gaussian envelope function. Locally modeled surface (§1.2, see §2.6) has been applied for visualization only. Square-root scaling is used to emphasize fainter structures.

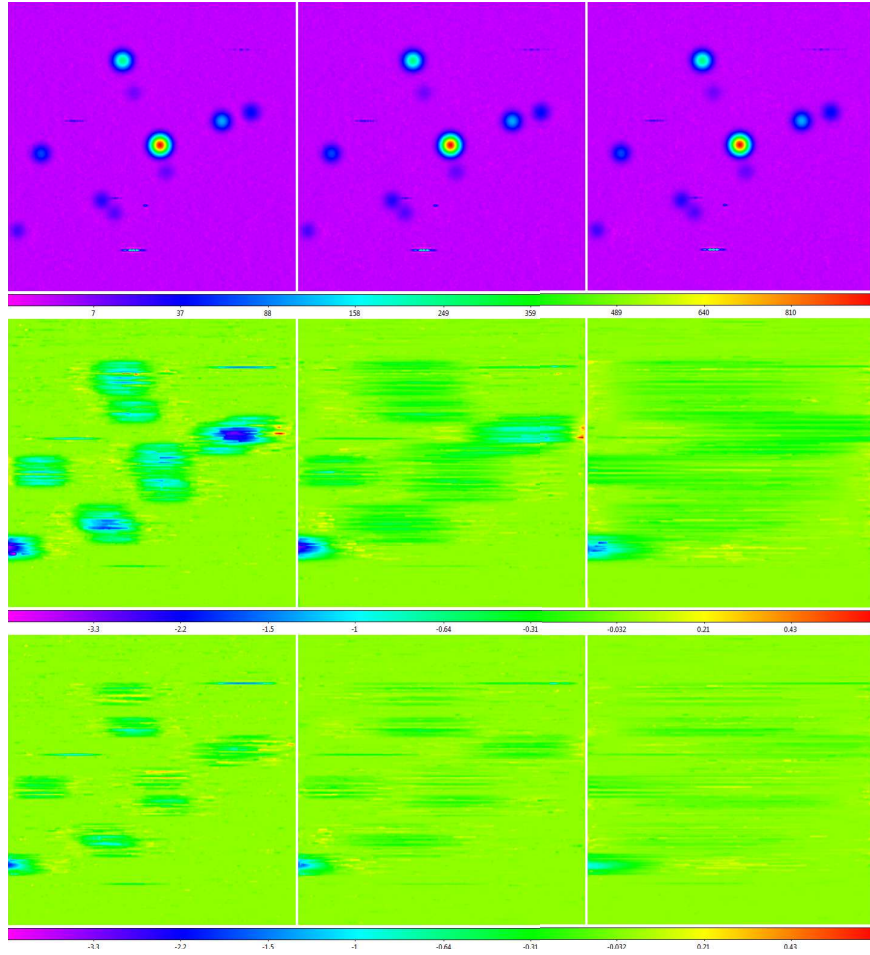


FIG. A.4.— **Top Row:** Data from Figure A.3 background-subtracted, with 6- (left), 12- (middle), and 24- (right) beamwidth scales (the map is 24 beamwidths across). **Middle Row:** Data from the top row (1) minus the data from Figure A.3 (residuals) and (2) minus the Gaussian random noise residuals from the bottom row of Figure A.2 (for greater clarity). Small-scale structure residuals are biased negative, but typically by at most  $\approx 1/2 - 1$  (left),  $\approx 1/4 - 1/2$  (middle), and  $\approx 1/8 - 1/4$  (right) of the noise level, and independently of the brightness of the proximal small-scale structure (point source or short-duration RFI). Larger values are possible when small-scale structures blend together into large-scale structures, in the scan direction, where the division between small and large scales is given by the background-subtraction scale. Larger values are also possible when small-scale structures occur near the ends of scans. Noise-level biases can be ignored for all but the lowest-S/N sources (see §3), and are further mitigated by our RFI-subtraction algorithm in §2.5, and by our large-scale structure algorithm in a following paper. **Bottom Row:** Same as the middle row, but for more-realistic, less-winged sources (given by Equation 9 with  $\theta_{RFI} = 1$  beamwidth and  $z_0 = 0$ ; see Figure 23); residuals are  $\approx 2 - 3$  times smaller in this case. Locally modeled surfaces (§1.2, see §2.6) have been applied for visualization only. Square-root and hyperbolic-arcsine scalings are used in the top and bottom two rows, respectively, to emphasize fainter structures.

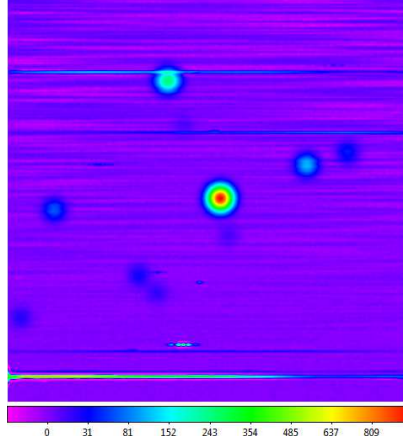


FIG. A.5.— Simulated data from Figure A.3 with added en-route drift and long-duration RFI. For the en-route drift, we use a sum of randomly phased sine functions. We linearly increase the maximum amplitude of the en-route drift from zero times the noise level at the bottom of the image to 12 times the noise level at the top of the image. For the long-duration RFI, we use a similarly constructed sum of sine functions, but plus a constant to ensure that it is always positive, and multiplied by a long-duration Gaussian envelope. The brightness of the long-duration RFI substantially exceeds the brightness of the en-route drift. Locally modeled surface (§1.2, see §2.6) has been applied for visualization only. Square-root scaling is used to emphasize fainter structures.

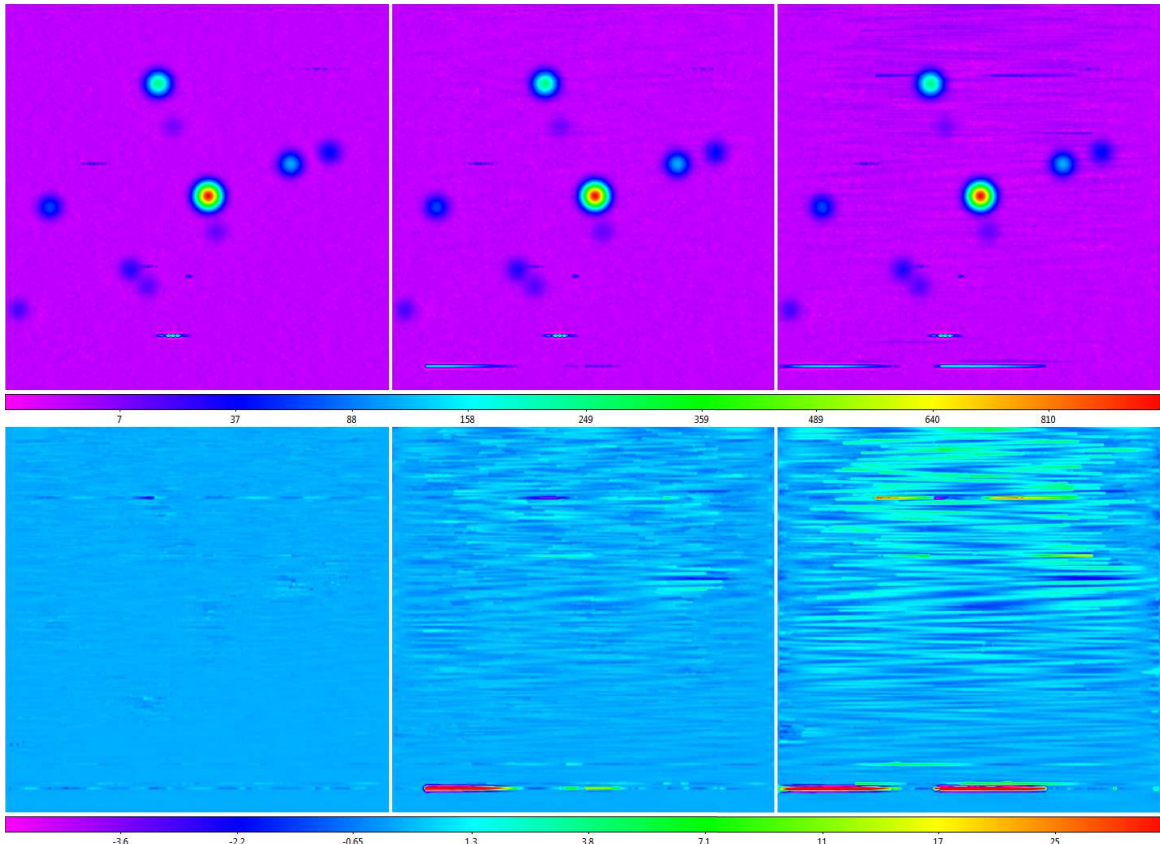


FIG. A.6.— **Top Row:** Data from Figure A.5 background-subtracted, with 6- (left), 12- (middle), and 24- (right) beamwidth scales (the map is 24 beamwidths across). **Bottom Row:** Data from the top row (1) minus the data from Figure A.3 (residuals) and (2) minus the Gaussian random noise residuals from the bottom row of Figure A.2, and the small-scale structure residuals from the middle row of Figure A.4 (for greater clarity). En-route drift and long-duration RFI are significantly reduced especially in the smaller background-subtraction scale maps (see Figure 14). These gains are furthered, and again significantly, by our RFI-subtraction algorithm in §2.5. Locally modeled surfaces (§1.2, see §2.6) have been applied for visualization only. Square-root and hyperbolic-arcsine scalings are used in the top and bottom rows, respectively, to emphasize fainter structures.

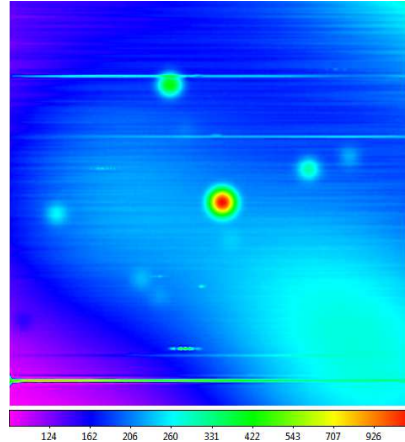


FIG. A.7.— Simulated data from Figure A.5 to which we have added large-scale astronomical and elevation-dependent signal. The large-scale astronomical signal is produced using a sum of 2D Gaussian distributions, each with a FWHM of  $\approx 12$  beamwidths. The elevation-dependent signal is modeled with a cosecant function. Locally modeled surface (§1.2, see §2.6) has been applied for visualization only. Hyperbolic arcsine scaling is used to emphasize fainter structures.

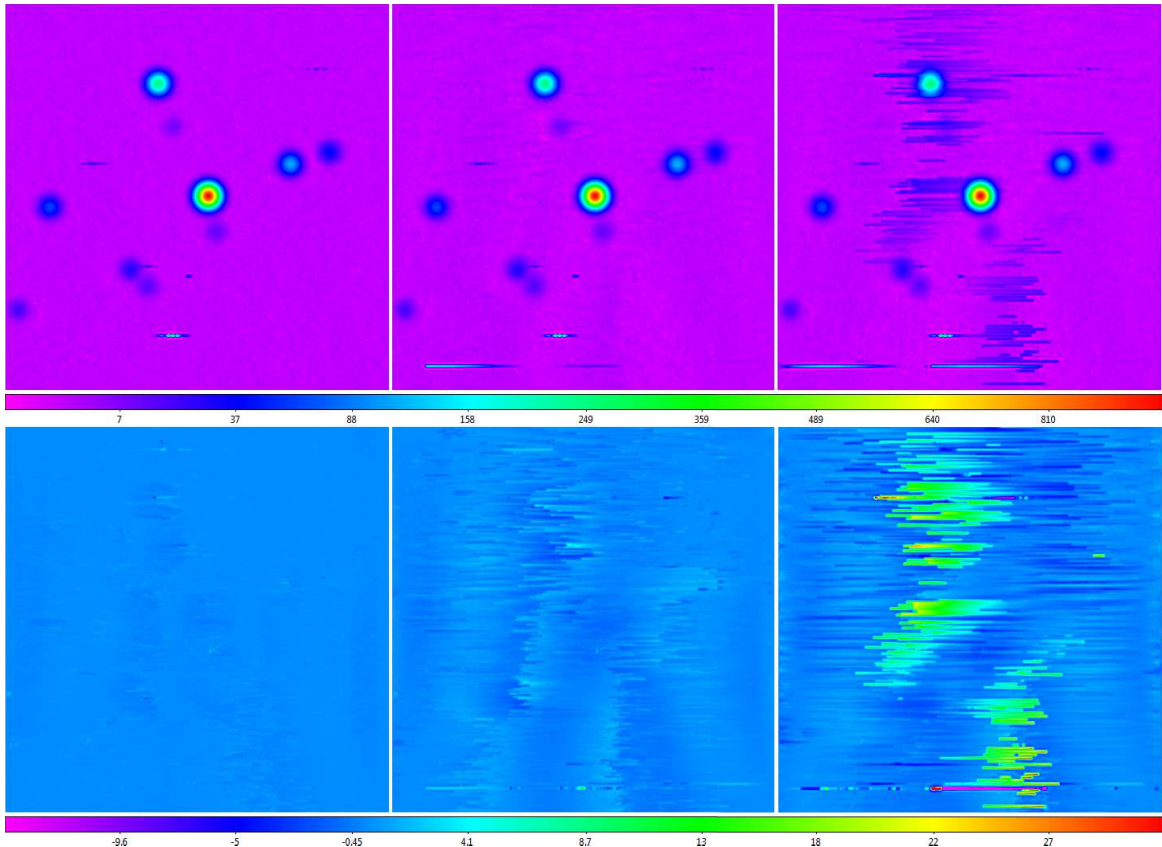


FIG. A.8.— **Top Row:** Data from Figure A.7 background-subtracted, with 6- (left), 12- (middle), and 24- (right) beamwidth scales (the map is 24 beamwidths across). **Bottom Row:** Data from the top row (1) minus the data from Figure A.3 (residuals) and (2) minus the Gaussian random noise residuals from the bottom row of Figure A.2, the small-scale structure residuals from the middle row of Figure A.4, and the 1D large-scale structure residuals from the bottom row of Figure A.6 (for greater clarity). Elevation-dependent signal is effectively eliminated. Large-scale astronomical signal is not eliminated, but is significantly reduced, especially in the smaller background-subtraction scale maps (Figure 14). These gains are furthered by our RFI-subtraction algorithm in §2.5. Locally modeled surfaces (§1.2, see §2.6) have been applied for visualization only. Square-root scaling is used in the top row to emphasize fainter structures.

## B. RFI-SUBTRACTION VERIFICATION

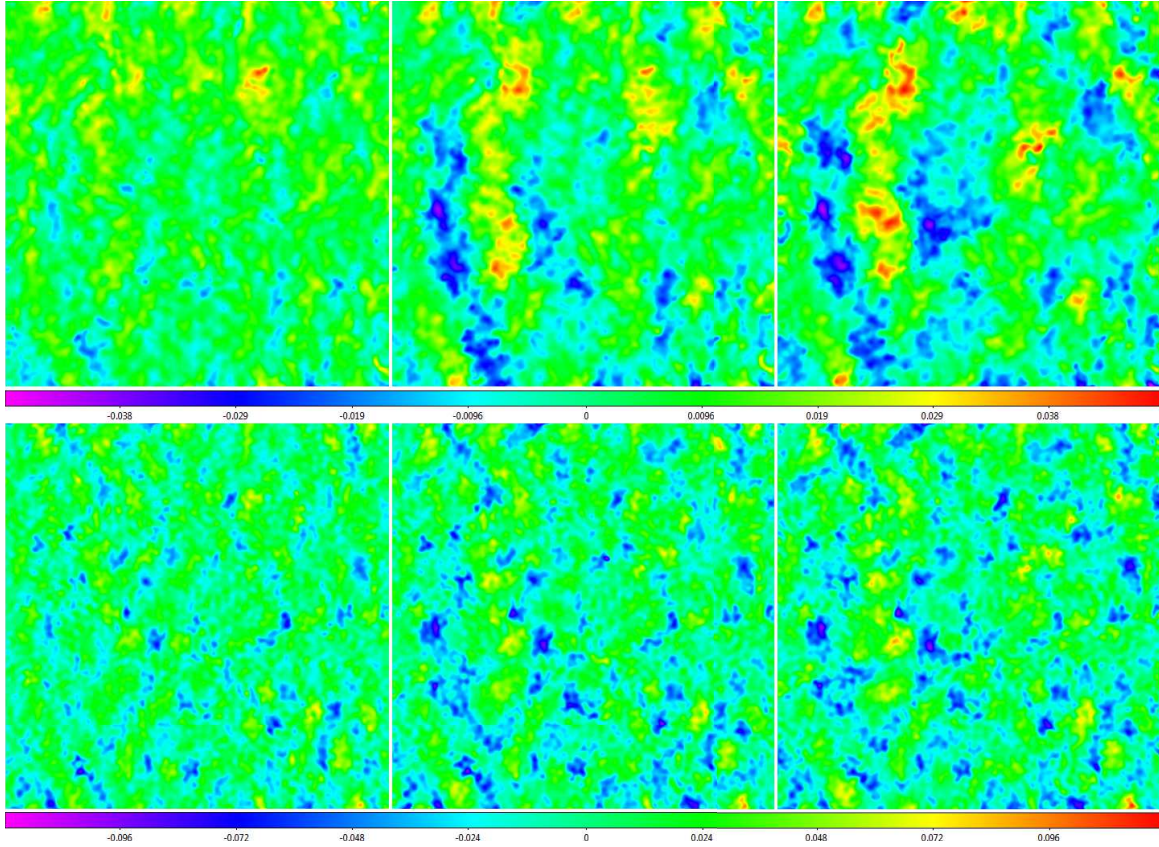


FIG. B.1.— Data from the top row of Figure A.2, corresponding to 6- (left column), 12- (middle column), and 24- (right column) beamwidth background-subtraction scales, RFI-subtracted, with 0.95- (top row) and 0.5- (bottom row) beamwidth scales. RFI-subtracted data are not biased high nor low. On the 0.95-beamwidth scale, the noise level of the RFI-subtracted data is  $\approx 1.1\%$  (left),  $\approx 1.3\%$  (middle), and  $\approx 1.4\%$  (right) of that of the background-subtracted data. On the smaller, 0.5-beamwidth scale, the noise level of the RFI-subtracted data is roughly twice that:  $\approx 2.5\%$  (left),  $\approx 2.8\%$  (middle), and  $\approx 3.0\%$  (right) of that of the background-subtracted data. Locally modeled surfaces (§1.2, see §2.6) have been applied for visualization only.

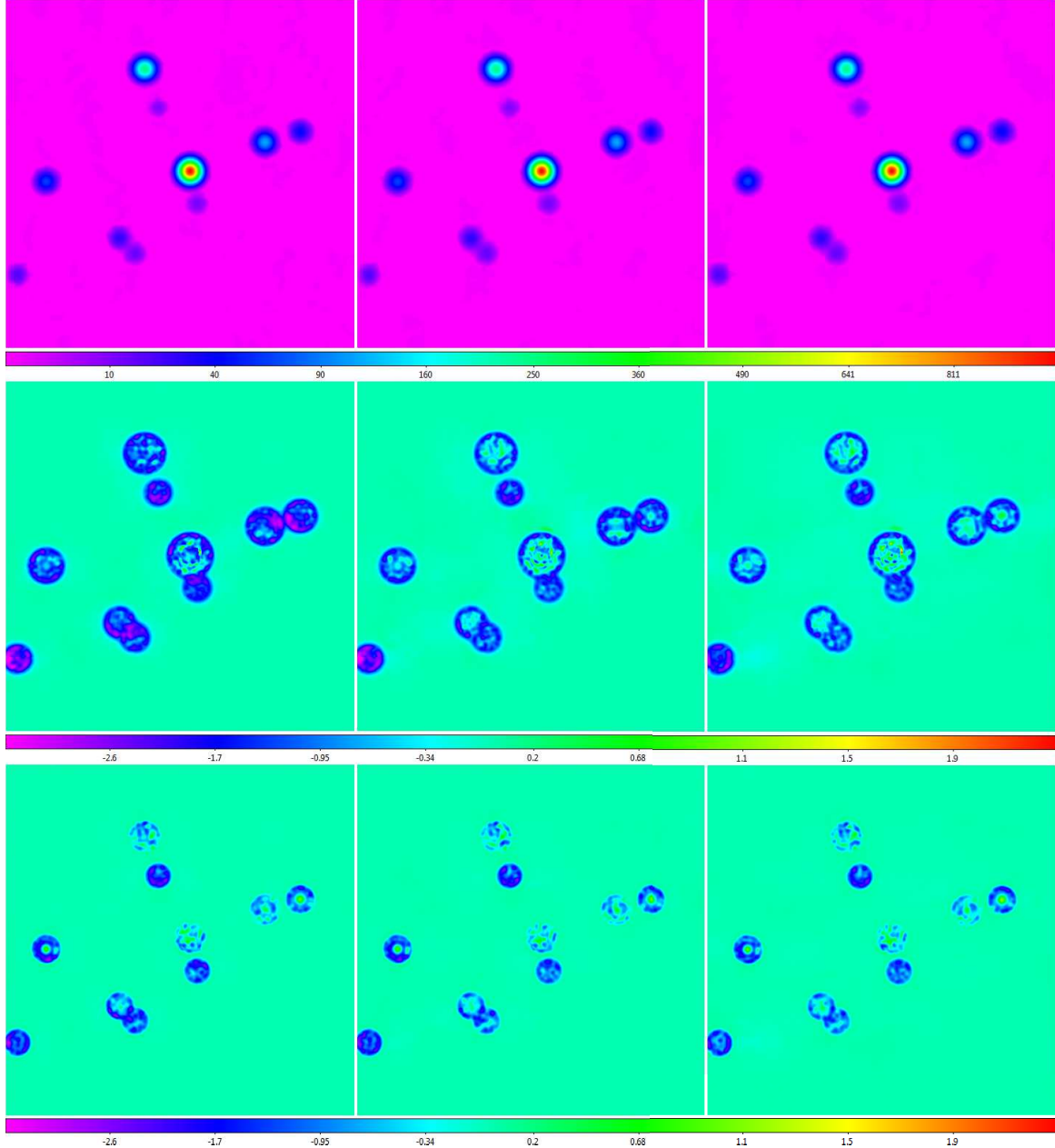


FIG. B.2.— **Top Row:** Data from the top row of Figure A.4, corresponding to 6- (left column), 12- (middle column), and 24- (right column) beamwidth background-subtraction scales, RFI-subtracted, with a 0.95-beamwidth scale. **Middle Row:** Data from the top row (1) minus the point sources from Figure A.3 (residuals) and (2) minus the Gaussian random noise residuals from the top row of Figure B.1 (for greater clarity). Short-duration RFI is effectively eliminated (Figure 14). Source residuals, overall, are biased negative, but (1) significantly less so than in Figure A.4, beyond where the sources intersect the noise level, (2) slightly more so at this boundary, corresponding to post-RFI subtraction sources having slightly clipped wings, and (3) at a similar level within this boundary, all relatively independently of the brightness of the source. **Bottom Row:** Same as the middle row, but for more-realistic, less-winged sources (given by Equation 9 with  $\theta_{RFI} = 1$  beamwidth and  $z_0 = 0$ ; Figure 23); residuals are again  $\approx 2 - 3$  times smaller in this case. Locally modeled surfaces (§1.2, see §2.6) have been applied for visualization only. Square-root scaling is used in the top row and squared scaling is used in the middle and bottom rows to emphasize fainter structures.

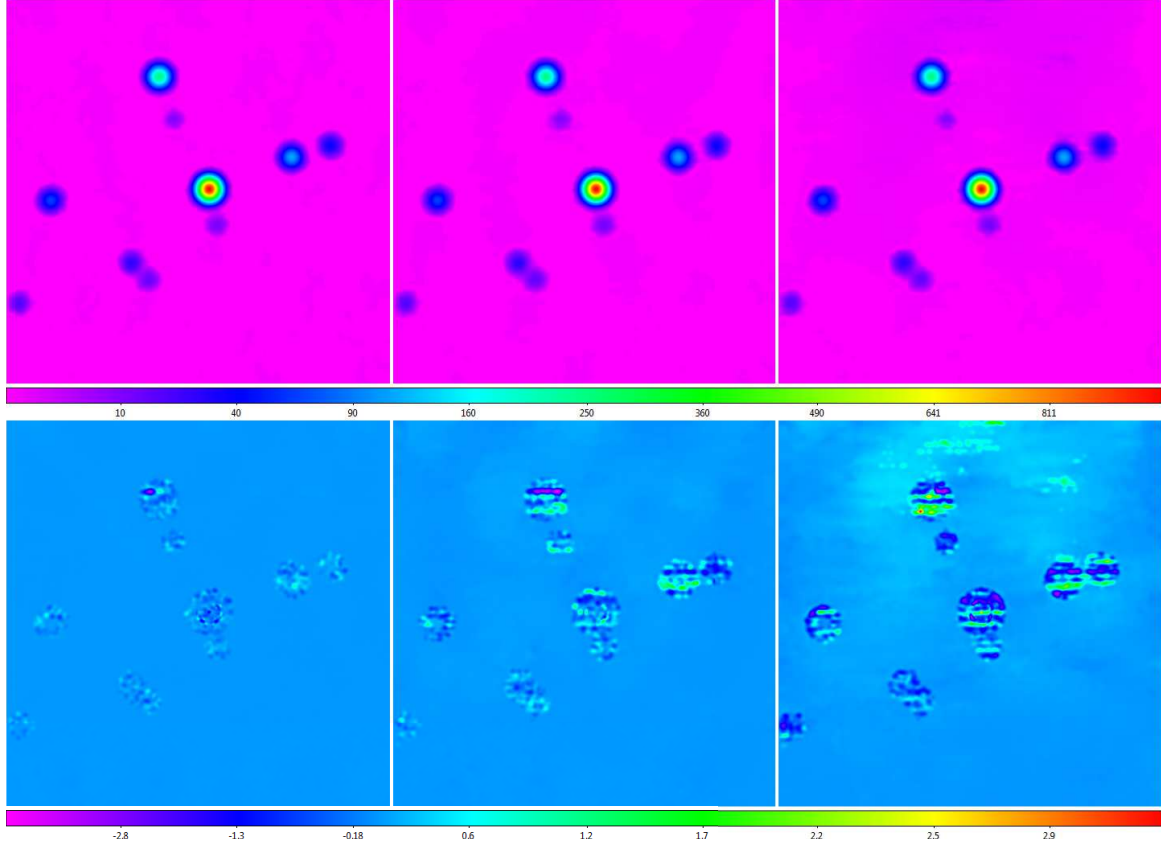


FIG. B.3.— **Top Row:** Data from the top row of Figure A.6, corresponding to 6- (left column), 12- (middle column), and 24- (right column) beamwidth background-subtraction scales, RFI-subtracted, with a 0.95-beamwidth scale. **Bottom Row:** Data from the top row (1) minus the point sources from Figure A.3 (residuals) and (2) minus the Gaussian random noise residuals from the top row of Figure B.1, and the small-scale structure residuals from the middle row of Figure B.2 (for greater clarity). Beyond where the sources intersect the noise level, en-route drift and long-duration RFI are effectively eliminated (Figure 14). Within these boundaries, the residuals are fairly consistent with the post-background subtraction residuals of Figure A.6; these are biased neither high nor low, and are noise-level. Locally modeled surfaces (§1.2, see §2.6) have been applied for visualization only. Square-root and hyperbolic-arcsine scalings are used in the top and bottom rows, respectively, to emphasize fainter structures.

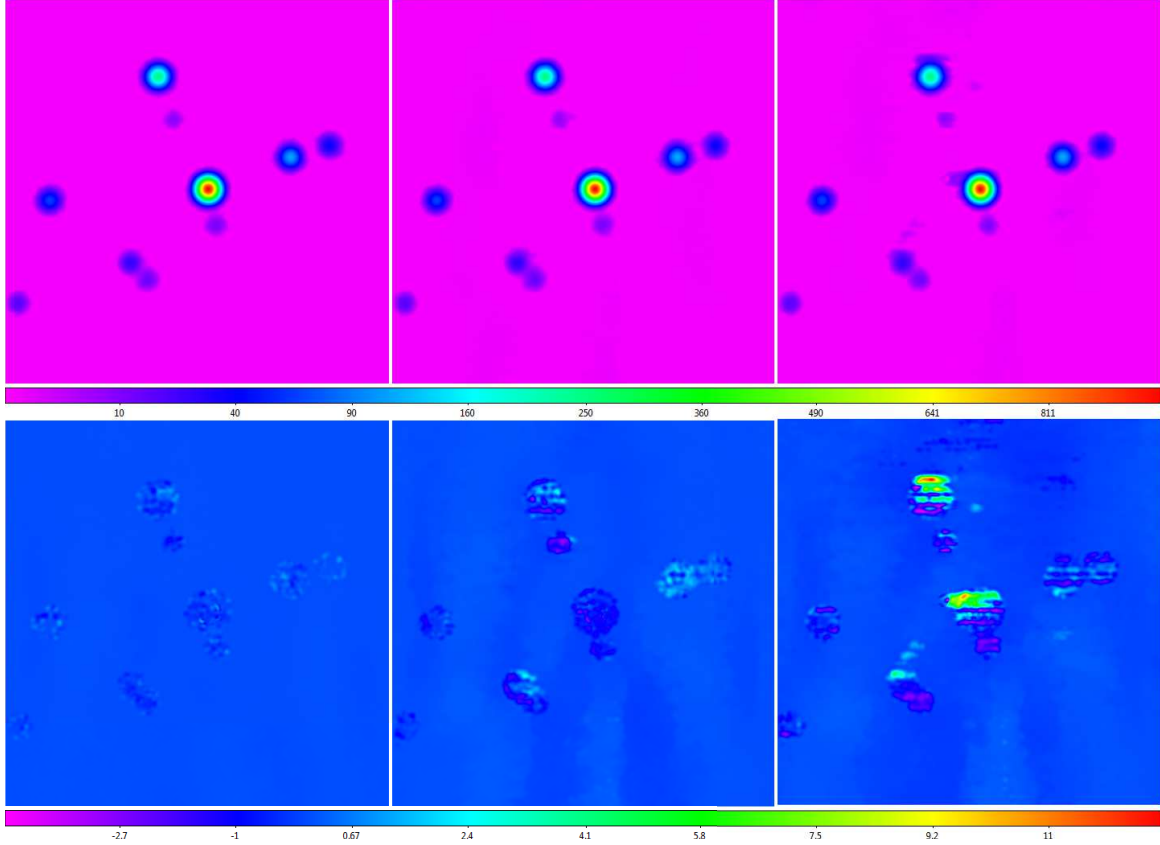


FIG. B.4.— **Top Row:** Data from the top row of Figure 23, corresponding to 6- (left column), 12- (middle column), and 24- (right column) beamwidth background-subtraction scales, RFI-subtracted, with a 0.95-beamwidth scale. **Bottom Row:** Data from the top row (1) minus the point sources from Figure A.3 (residuals) and (2) minus the Gaussian random noise residuals from the top row of Figure B.1, the small-scale structure residuals from the middle row of Figure B.2, and the 1D large-scale structure residuals from the bottom row of Figure B.3 (for greater clarity). Elevation-dependent signal is effectively eliminated (Figure 14). Large-scale astronomical signal is not eliminated, but is significantly reduced, especially in the smaller background-subtraction scale maps (Figure 14). Locally modeled surfaces (§1.2, see §2.6) have been applied for visualization only. Square-root and hyperbolic-arcsine scalings are used in the top and bottom rows, respectively, to emphasize fainter structures.

## REFERENCES

- Abbas, M., Layden, A., Guldenschuh, K., et al. 2015, AJ, 149, A40
- Abbott, B. P., Abbott, R., Abbott, T. D., et al. 2017a, ApJ, 848, L12
- Abbott, B. P., Abbott, R., Abbott, T. D., et al. 2017b, Nature, 551, 85
- Awiphan, S., Kerins, E., Pichadee, S., et al. 2016, MNRAS, 463, 2574
- Baars, J. W. M., Genzel, R., Pauliny-Toth, I. I. K., & Witzel, A. 1974, A&A, 61, 99
- Barbarino, C., Dall’Ora, M., Botticella, M. T., et al. 2015, MNRAS, 448, 2312
- Bardho, O., Gendre, B., Rossi, A., et al. 2016, MNRAS, 459, 508
- Barlow, B. N., Dunlap, B. H., Clemens, J. C., et al. 2010, MNRAS, 403, 324
- Barlow, B. N., Dunlap, B. H., Clemens, J. C., et al. 2011, MNRAS, 414, 3434
- Barlow, B. N., Kilkenny, D., Drechsel, H., et al. 2013, MNRAS, 430, 22
- Barlow, B. N., Kilkenny, D., Geier, S., et al. 2017, PASP, 129, A054202
- Berger, T. A. 2015, UNC Chapel Hill Undergraduate Honors Thesis Collection
- Bickel, D. R., & Fruhwirth, R. 2006, Computational Statistics and Data Analysis, 50, 3500
- Blank, D. L., Feliz, D., Collins, K. A., et al. 2018, ApJ, submitted
- Boudreault, T. M., Barlow, B. N., Fleming, S. W., et al. 2017, ApJ, 848, 171
- Bowyer, O., & Meredith, W. 1963, Green Bank Observer, Apr. 30, 2
- Braga-Ribas, F., Sicardy, B., Ortiz, J. L., et al. 2013, ApJ, 773, A26
- Braga-Ribas, F., Sicardy, B., Ortiz, J. L., et al. 2014, Nature, 508, 72
- Brozovic, M., Benner, L. A. M., Nolan, M. C., et al. 2011, Icarus, 216, 241
- Bufano, F., Pian, E., Sollerman, J., et al. 2012, ApJ, 753, A67
- Cano, Z., Bersier, D., Guidorzi, C., et al. 2011, MNRAS, 413, 669
- Cenko, S. B., Frail, D. A., Harrison, F. A., et al. 2011, ApJ, 732, A29
- Chauvenet, W. 1863, A Manual of Spherical and Practical Astronomy, Vol. 2 (Philadelphia, PA: J. B. Lippincott Company)
- Cosin, J. 1570, Carte cosmographique ou universelle description du monde avec le vrai traict des vents
- Czesla, S., Schroter, S., Wolter, U., et al. 2012, A&A 539, A150
- Dai, X., Halpern, J. P., Morgan, N. D., et al. 2007, ApJ, 658, 509
- Dall’Ora, M., Botticella, M. T., Pumo, M. L., et al. 2014, ApJ, 787, A139
- De Pasquale, M., Oates, S. R., Racusin, J. L., et al. 2016, MNRAS, 455, 1027
- Descamps, P., Marchis, F., Durech, J., et al. 2009, Icarus, 203, 88
- Dias-Oliveira, A., Sicardy, B., Lellouch, E., et al. 2015, ApJ, 811, A53
- Dutton, D. A., Reichart, D. E., Martin, J. R., et al. 2018, in prep.
- Emerson, D. T., & Grave, R. 1988, A&A, 190, 353
- Fischer, D. A., Laughlin, G., Marcy, G. W., et al. 2006, ApJ, 637, 1094
- Folatelli, G., Bersten, M. C., Kuncarayakti, H., et al. 2014, ApJ, 792, A7
- Foley, R. J., Rest, A., Stritzinger, M., et al. 2010, AJ, 140, 1321
- Foley, R. J., Kromer, M., Howie, M. G., et al. 2012, ApJ, 753, L5
- Foley, R. J., Challis, P. J., Chornock, R., et al. 2013, ApJ, 767, A57
- Fraser, M., Inserra, C., Jerkstrand, A., et al. 2013, MNRAS, 443, 1312
- Friis, M., De Cia, A., Krhler, T., et al. 2015, MNRAS, 451, 167
- Fuchs, J. T., Dunlap, B. H., Dennihy, E., et al. 2016, MNRAS, 462, 2382
- Goyal, A., Stawarz, L., Zola, S., et al. 2017, ApJ, submitted
- Guinan, E. F., Engle, S. G., & Durbin, A. 2016, ApJ, 821, A81
- Gutierrez, C. P., Gonzalez-Gaitan, S., Folatelli, G., et al. 2016, A&A, 590, A5
- Gvaramadze, V. V., Kniazev, A. Y., Miroshnichenko, A. S., et al. 2012, MNRAS, 421, 3325
- Haislip, J. B., Nysewander, M. C., Reichart, D. E., et al. 2006, Nature, 440, 181
- Haslam, C. G. T., Quigley, M. J. S., & Salter, C. J. 1970, MNRAS, 147, 405
- Haslam, C. G. T., Wilson, W. E., Graham, D. A., & Hunt, G. C. 1974, A&AS, 13, 359
- Haslam, C. G. T., Klein, U., Salter, C. J., et al. 1981, A&A, 100, 209
- Helminiak, K. G., Konacki, M., Zloczewski, K., et al. 2011, A&A, 527, A14
- Helminiak, K. G., Konacki, M., RoZyczka, M., et al. 2012, MNRAS, 425, 1245
- Helminiak, K. G., Graczyk, D., Konacki, M., et al. 2015, MNRAS, 448, 1945
- Hutchens, Z. L., Barlow, B. N., Soto, A. V., et al. 2017, Open Astronomy, 26, 252
- Inserra, C., Smartt, S. J., Scalzo, R., et al. 2014, MNRAS, 437, L51
- Inserra, C., Fraser, M., Smartt, S. J., et al. 2016, MNRAS, 459, 2721
- de Jaeger, T., Anderson, J. P., Pignata, G., et al. 2015, ApJ, 807, A63
- Jin, Z.-P., Covino, S., Della Valle, M., et al. 2013, ApJ, 774, A114
- Khokhlov, S. A., Miroshnichenko, A. S., Mennickent, R., et al. 2017, ApJ, 835, A53
- Khokhlov, S. A., Miroshnichenko, A. S., Zharikov, S. V., et al. 2018, ApJ, in press
- Kenworthy, M. A., Lacour, S., Kraus, A., et al. 2015, MNRAS, 446, 441
- Kuhn, R. B., Rodriguez, J. E., Collins, K. A., et al. 2016, MNRAS, 459, 4281
- Kriwattanawong, W., Sarotsakulchai, T., Maungkorn, S., et al. 2018, New Astronomy, 61, 1
- Layden, A. C., Broderick, A. J., Pohl, B. L., et al. 2010, PASP, 122, 1000
- Liu, X., Yang, P. P., Liu, J., et al. 2017, MNRAS, 469, 2457
- Lockman, F. J., Ghigo, F. D., & Balser, D. S. 2007, *But it was Fun: the first forty years of radio astronomy at Green Bank* (Green Bank, WV: National Radio Astronomy Observatory), 90
- Lubin, J. B., Rodriguez, J. E., Zhou, G., et al. 2017, ApJ, 844, 134
- Ma, C., Arias, E. F., Ebanks, T. M., et al. 1998, AJ, 116, 516
- Mangum, J. G., Emerson, D. T., & Greisen, E. W. 2007, A&A 474, 679
- Maples, M. P., Reichart, D. E., Berger, T. A., et al. 2017, ApJS, submitted
- Marchis, F., Enriquez, J. E., Emery, J. P., et al. 2012, Icarus, 221, 1130
- Martin-Carrillo, A., Hanlon, L., Topinka, M., et al. 2014, A&A, 567, A84
- Maund, J. R., Fraser, M., Smartt, S. J., et al. 2013, MNRAS, 431, L102
- Melandri, A., Covino, S., Zaninoni, E., et al. 2017, A&A, 607, A29
- Meng, H. Y. A., Su, K. Y. L., Rieke, G. H., et al. 2014, Science, 345, 1032
- Meng, H. Y. A., Su, K. Y. L., Rieke, G. H., et al. 2015, ApJ, 805, A77
- Milisavljevic, D., Margutti, R., Soderberg, A. M., et al. 2013, ApJ, 767, A71
- Miroshnichenko, A. S., Manset, N., Zharikov, S. V., et al. 2014, Advances in Astronomy, 2014, A130378
- Morgan, A. N., Perley, D. A., Cenko, S. B., et al. 2014, MNRAS, 440, 1810
- Neustroev, V. V., Marsh, T. R., Zharikov, S. V., et al. 2017, MNRAS, 467, 597
- Norrod, R. D., Behrens, G. H., Ghigo, F. D., & Levin, B. J. 1994, Proc. IEEE, 82, 768
- Nysewander, M. C., Reichart, D. E., Crain, J. A., et al. 2009, ApJ, 693, 1417
- Osterman Meyer, A., Miller, H. R., Marshall, K., et al. 2008, AJ, 136, 1398
- Pala, A. F., Gansicke, B. T., Townsley, D., et al. 2017, MNRAS, 466, 2855
- Pastorello, A., Cappellaro, E., Inserra, C., et al. 2013, ApJ, 767, A1
- Pignata, G., Stritzinger, M., Soderberg, A., et al. 2011, ApJ, 728, A14
- Pravec, P., Vokrouhlický, D., Polishook, D., et al. 2010, Nature, 466, 1085
- Pravec, P., Scheirich, P., Vokrouhlický, D., et al. 2012, Icarus, 218, 125
- Pravec, P., Scheirich, P., Durech, J., et al. 2014, Icarus, 233, 48
- Pravec, P., Scheirich, P., Kusnirak, P., et al. 2016, Icarus, 267, 267
- Prentice, S. J., Ashall, C., Mazzali, P. A., et al. 2017, MNRAS, submitted
- Reed, M. D., Kilkenny, D., O’Toole, S., et al. 2012, MNRAS, 421, 181
- Reed, P. A., McCluskey, G. E., Kondo, Y., et al. 2010, MNRAS, 401, 913
- Reichart, D. E., & Stephens, A. W. 2000, ApJ, 537, 904
- Reichart, D., Nysewander, M., Moran, J., et al. 2005, Nuovo Cimento C, 28, 767
- Sarty, G. E., Pilecki, B., Reichart, D. E., et al. 2011, Research in Astronomy and Astrophysics, 11, 947
- Savanevych, V. E., Khlamov, S. V., Vavilova, I. B., et al. 2018, A&A, 609, A54

- Schaefer, B. E., Pagnotta, A., LaCluyze, A., et al. 2011, ApJ, 742, A113
- Sieber, W., Haslam, C. G. T., & Salter, C. J. 1979, A&A, 74, 361
- Sofue, Y., & Reich, W. 1979, A&AS, 38, 251
- Strader, J., Chomiuk, L., Cheung, C. C., et al. 2015, ApJ, 804, L12
- Stritzinger, M. D., Hsiao, E., Valenti, S., et al. 2014, A&A, 561, A146
- Swihart, S. J., Strader, J., Johnson, T. J., et al. 2017, ApJ, 851, A31
- Takats, K., Pumo, M. L., Elias-Rosa, N., et al. 2014, MNRAS, 438, 368
- Takats, K., Pignata, G., Pumo, M. L., et al. 2015, MNRAS, 450, 3137
- Takats, K., Pignata, G., Bersten, M., et al. 2016, MNRAS, 460, 3447
- Tartaglia, L., Fraser, M., Sand, D. J., et al. 2017, ApJ, 836, L12
- Tartaglia, L., Sand, D. J., Valenti, S., et al. 2018, ApJ, 853, A62
- Thompson, S. E., Montgomery, M. H., von Hippel, T., et al. 2010, ApJ, 714, 296
- Tovmassian, G., Gonzalez-Buitrago, D., Zharkov, S., et al. 2016, ApJ, 819, A75
- Tovmassian, G., Gonzalez-Buitrago, D., Buitrago, D., et al. 2017, A&A, 608, 36
- Trotter, A. S., Reichart, D. E., Egger, R. E., et al. 2017, MNRAS, 469, 1299
- Updike, A. C., Haislip, J. B., Nysewander, M. C., et al. 2008, ApJ, 685, 361
- Valenti, S., Fraser, M., Benetti, S., et al. 2011, MNRAS, 416, 3138
- Valenti, S., Yuan, F., Taubenberger, S., et al. 2014, MNRAS, 437, 1519
- Valenti, S., Sand, D., Yang, S. et al. 2017, ApJ, 848, L24
- Valtonen, M. J., Zola, S., Ciprini, S., et al. 2016, ApJ, 819, L37
- Wehrung, M., Layden, A., Rogel, A., et al. 2013, Information Bulletin on Variable Stars, 6071
- Winkel, B., Floer, L., & Kraus, A. 2012, A&A, 547, 119
- Yang, S., Valenti, S., Cappellaro, E. et al. 2017, ApJ, 851, 48
- Zola, S., Valtonen, M., Bhatta, G., et al. 2016, Galaxies, 4, A41
- Zola, S., Szkody, P., Ciprini, S., et al. 2017, AJ, 154, A276